NUMERICAL SIMULATION OF THREE-DIMENSIONAL COMBINED CONVECTIVE RADIATIVE HEAT TRANSFER IN RECTANGULAR CHANNELS

A Dissertation

by

MIN SEOK KO

Submitted to the Office of Graduate Studies of
Texas A&M University
in partial fulfillment of the requirements for the degree of

DOCTOR OF PHILOSOPHY

December 2007

Major Subject: Mechanical Engineering

NUMERICAL SIMULATION OF THREE-DIMENSIONAL COMBINED CONVECTIVE RADIATIVE HEAT TRANSFER IN RECTANGULAR CHANNELS

A Dissertation

by

MIN SEOK KO

Submitted to the Office of Graduate Studies of
Texas A&M University
in partial fulfillment of the requirements for the degree of

DOCTOR OF PHILOSOPHY

Approved by:

Chair of Committee,	N. K. Anand
Committee Members,	Kalyan Annamalai
	Sai Lau
	Hamn-Ching Chen
Head of Department,	Dennis O'Neal

December 2007

Major Subject: Mechanical Engineering

ABSTRACT

Numerical Simulation of Three-Dimensional Combined Convective Radiative Heat Transfer in Rectangular Channels. (December 2007)

Min Seok Ko, B.S., Inha University, South Korea;

M.S., Texas A&M University

Chair of Advisory Committee: Dr. N. K. Anand

This dissertation presents a numerical simulation of three-dimensional flow and heat transfer in a channel with a backward-facing step. Flow was considered to be steady, incompressible, and laminar. The flow medium was treated to be radiatively participating. Governing momentum equations, energy equation, and the radiative equation were solved by a finite volume method. Extensive validation studies were carried out. As part of the validation study, three-dimensional combined convection and radiation in a rectangular channel without a backward-facing step was studied. The SIMPLE algorithm was used to link pressure and velocity fields. The combined convective-radiative heat transfer were studied by varying three parameters, i.e. optical thickness (τ_H=0.1, 0.2, and 0.4) and scattering albedo (ω=0, 0.25, 0.5, 0.75 and 1). Variation of thermophysical properties with temperature was considered in this study. In this work consideration was given only to cooling. Effects of those radiative parameters on velocity, bulk temperature, and Nusselt number are presented in detail. The fluid with a hot inlet compared to a cold wall was cooled in a relatively short distance from the

channel inlet because of the radiation effect. The thermal penetration decreased with a decrease in optical thickness and an increase in scattering albedo. Thermal penetration increased with increasing optical thickness and decreasing scattering albedo. The reattachment length varied with temperature due to variation of thermophysical properties with temperature.

To my father, Jeong-Hwan Ko in heaven:

Without whom I could have never come so far

ACKNOWLEDGEMENTS

First, I would like to thank my advisor, Dr. N. K. Anand, for spending his valuable time in guiding me throughout my graduate studies. I also want to thank my committee members, Dr. Kalyan Annamalai, Dr. Sai Lau, and Dr. Hamn-Ching Chen, for their guidance throughout my research.

I want to express many thanks to my mother in Korea for her belief in me and support beyond measure. It is due to her immense help that I have been able to reach this position.

I am also deeply thankful to Ms. Teresa Wright for her editorial help in preparing this dissertation.

Finally, I must thank my wife, Sunjeong Oh, from the bottom of my heart for her endless love, endurance, and understanding during my life in Texas A&M University.

NOMENCLATURE

AR	aspect ratio
C_j	expansion coefficient
C_p	specific heat of fluid, $J/kg \cdot K$
D_{cx}, D_{cy}, D_{cz}	defined quantities, Eqs. (3.38) - (3.40)
ER	expansion ratio
G	incident radiation, W/m^2
H	channel height, m
I	radiative intensity, $W/m^2 \cdot sr$
I_b	blackbody intensity, $W/m^2 \cdot sr$
k	thermal conductivity, $W/m \cdot K$
l	step height, m
L	channel length, m
M	total number of ordinates direction
n_x, n_y, n_z	unit vector for x,y,z directions
Nu_c	convective Nusselt number, Eq.(5.5)
$Nu_{x,p}$	peripheral average local Nusselt number
Nu_r	radiative Nusselt number, Eq. (5.6)
Nu_t	total Nusselt number, Eq. (5.7)
N_φ	number of control angles in φ direction

N_θ	number of control angles in θ direction
p	pressure, N/m^2
P_j	Legendre polynomial
q	radiative heat flux, W/m^2
Re	Reynolds number ($=U_0 H/\nu$)
R_ϕ	residual for velocity components
R_p	residual for pressure
s	step height, m
$\hat{s}$	traveled distance
S	source function
S_m^l	modified source function
T	temperature, K
T_b	bulk temperature, K
T_{in}	inlet temperature, K
T_w	wall temperature, K
U_0	bulk inlet velocity, m/s
x,y,z	coordinate directions
W	channel width, m
Xu	non-dimensional reattachment length from the step wall

Greek

β	extinction coefficient
β_m^l	modified extinction coefficient
Γ	diffusion coefficient
ΔA	area of control volume face, m^2
$\Delta\Omega$	solid angle, sr
Δv	control volume, m^3
ε	emissivity
ε_w	wall emissivity
κ	absorption coefficient, m^{-1}
ν	kinematic viscosity, m^2 / s
Φ	scattering phase function
$\Phi^{l'l}$	average energy scattered form control angle l' to l
φ	azimuthal angle, rad
ϕ	velocity components, m/s
ρ	density, kg / m^3
$\widehat{\rho}$	reflectivity
σ	scattering coefficient
τ_H	optical thickness
θ	polar angle, rad
θ_b	non-dimensional bulk mean temperature, Eq. (5.4)

ω	scattering albedo
Ψ	scattering angle, *rad*

Subscripts

b	bottom (surface between nodes)
B	bottom neighbor node
e	east (surface between nodes)
E	east neighbor node
n	north (surface between nodes)
N	north neighbor node
nb	neighbor points
P	central grid point
s	south (surface between nodes)
S	south neighbor node
t	top (surface between nodes)
T	top neighbor node
w	west (surface between nodes)
W	west neighbor node

Superscript

l', l	l' and l direction in control angle
*	previous value
,	pressure correction

TABLE OF CONTENTS

Page

LIST OF FIGURES

Page

LIST OF TABLES

1. INTRODUCTION AND LITERATURE REVIEW

1.1 Background

Combined mode of heat transfer for a radiatively participating medium is important in high temperature applications such as glass manufacturing, oil or gas-fired boilers, nuclear reactors, and industrial furnaces. The analysis of these systems is complicated by the presence of radiation. In high temperature applications the fluids are usually a participating media which can absorb and emit thermal radiation. Therefore, we should consider not only convective flow and heat transfer but also radiative heat transfer of participating media.

It has been of interest to many researchers to investigate the fluid flow and heat transfer of combined convective radiative mode. Especially, there have been many efforts to solve thermal radiation in combined heat transfer applications because the solution of the radiative transfer equation is difficult to obtain even for simple geometry. Among many developed methods to solve the radiative transfer equation, it is desirable to choose the finite volume method which can share the same computational grid and concept during the discretization procedure.

This dissertation presents the numerical procedures to study three-dimensional combined convective radiative heat transfer using a finite volume method in rectangular channels. In particular, combined convection and radiation in a three-dimensional rectangular channel with and without a backward-facing step is considered. Study of

---

This dissertation follows the style of *Numerical Heat Transfer*.

combined convection and radiation in a straight rectangular channel serves to validate finite volume formulation. Flow over a backward-facing step in a rectangular channel includes rich flow physics. The flow behavior includes through flow, flow separation, reattachment, and flow recirculation. Thus, this flow geometry is regarded as the "benchmark problem". The results of this study will serve as a benchmark for further investigations in the area of combined convection and radiation.

1.2 Literature Review

Over the past decade, a number of combined mode heat transfer analysis in channel flow have been reported in literature.

Wassel [1] presented the result for laminar and turbulent flow with combined non-gray radiation and thermal diffusion. He solved the governing equation by the Galerkin method for laminar flow and by a finite difference method for turbulent flow.

Im and Ahluwalia [2 and 3] studied combined convective and radiative heat transfer in a rectangular duct and a circular duct by solving simultaneously the flow and radiative transport equations. They used the assumption of parabolic flow and the moment method to simplify the fluid and radiative heat transfer equation respectively. Also, they used the exponential wideband model and the Mie theory for determining the spectral absorption and scattering coefficients of the particles. One of their foundations was that the combined contribution of carbon dioxide and water vapor to radiative heat transfer was less than the sum of individual contributions of carbon dioxide and water

vapor when present alone. It was observed in their work that the radiation caused the thermal boundary to become thicker than the momentum boundary layer.

Kassemi and Chung [4] examined the combined effects of forced convection and radiation in a fully developed flow in a two-dimensional parallel plate channel by using an element-to-node approach. The effects of Peclet number, gas and wall conduction to radiation parameters, and optical thickness on gas and wall temperature distribution were investigated.

Kim and Lee [5] presented a thermally developing Poiseuille flow with anisotropic scattering medium between two parallel plates. They considered gray absorbing, emitting, and anisotropic fluid flow. They found that results obtained from one-dimensional treatment of the radiative transfer were shown to be quite different from those obtained from two-dimensional radiation analysis. They showed that the reflecting walls enhanced the fluid thermal development significantly even with small radiative energy input.

Simultaneously developing laminar flow and heat transfer with convection and radiation in a smooth tube was studied by Seo et al. [6]. They solved the radiative heat transfer equation by the P-1 approximation and the exponential wideband model. They assumed the gas physical properties to be constant. They showed that the bulk mean temperature variation, the temperature profiles, and the Nusselt number distributions for non-gray gas mixtures are very different from those for pure convection. Also, they found that the heat transfer characteristics of non-gray gas mixtures depend strongly on

the mole fraction of non-gray gases, and a small amount of radiating gases can change the heat transfer significantly.

Kim and Baek [7] investigated a combined heat transfer mode of conduction, convection, and radiation in a two-dimensional gradually expanding channel. They developed a program to study the radiation in a curvilinear coordinate system. They showed that the thermal characteristics were affected by various parameters such as Prandtl number, conduction to radiation parameter, wall emissivity, and scattering albedo. They also mentioned that faster heating resulting in the lower adverse pressure gradient led to a decrease in the reattachment length. They reported that temperature distribution was also influenced by radiation, depending on the absorption coefficient.

A numerical study of the interaction between thermal radiation and laminar mixed convection for ascending flows of participating gases in vertical tubes are presented by Sediki et al. [8]. The radiative properties of real gas such as H_2O , CO_2 , and mixtures were considered. They found that the propagation of radiation towards the central region of the duct tends to increase the centerline velocity and decreases the friction factor, and results in a significant increase of the critical *Gr/ Re* ratio corresponding to reverse flow occurrence. They also mentioned that radiation had a small effect on the regime of reverse flow occurrence in an optically thin region.

More recently, Chiu et al. [9] presented numerically the mixed convective heat transfer with radiation effects in a horizontal duct. They used the discrete ordinates method to solve the radiative transfer equation and the vorticity-velocity method to solve

the momentum and energy equations simultaneously. The effects of thermal buoyancy and radiation on temperature, friction factor, and Nusselt number were presented.

Chai et al. [10] presented a numerical analysis for laminar radiating fluid over a two-dimensional backward-facing step geometry. They assumed that the flow field was decoupled from the energy field by treating the thermophysical properties to be constant. They presented various effects related to combined mode of heat transfer, such as conduction to radiation parameter, Reynolds number, scattering albedo, anisotropic scattering phase function, and optical thickness. They found that the shape of the scattering phase function had insignificant effects on the temperature distribution. They considered the backward-facing step but only focused on isotherms as a result because the velocity fields were not affected from temperature due to the constant property assumption.

It is also important to choose a useful method for solving a radiation heat transfer equation. The solution method should be able to handle the complexity encountered in combined convective radiative mode conveniently and accurately. During the past few decades, numerous radiation models have been developed to calculate radiative heat transfer. Many of those models are based on the solution of the radiative transfer equation.

The Hottel's zonal method was proposed by Hottel and Cohen [11] for solving radiative heat transfer with absorbing, emitting, non-scattering gray medium with constant absorption coefficient. In this method, the enclosure was subdivided into a finite number of volumes and surface area zones with uniform temperature and

properties. Then, surface-volume and volume-volume "exchange areas" were calculated. An energy balance was performed on each volume to give a set of nonlinear equations. This procedure leads to a set of simultaneous equations for unknown temperature or heat fluxes. One of the disadvantages of the zonal method is the complicated work needed in the evaluation of the "exchange areas". Naraghi and Kassemi [12] presented various improvements on those problems and proposed the procedure to implement an unstructured grid. Accuracy of the zonal method can be improved by increasing the number of zones, but it requires inversion of a large matrix. Despite several improvements and approaches, the evaluation of "exchange areas" is still difficult to evaluate in irregular geometries.

The Monte Carlo method was introduced by Howell and Perlmutter [13]. The Monte Carlo method solves the thermal radiation equation by tracing the history of a finite number of photons from their points of emission to their points of absorption. For a finite number of photons random numbers are generated and used to determine the travel distance. The Monte Carlo method has an advantage of applying to complicated problems with relative ease. The disadvantage of the Monte Carlo method is that it entailes a statistical error. Also, it can be time-consuming because this procedure is repeated until all rays are absorbed.

The method of spherical harmonics is also called P_N approximation. This approximation was proposed by Jeans [14]. Menguc and Viskanta [15 and 16] introduced P_1 and P_2 formulations for absorbing, emitting, and anisotropically scattering gas in two-dimensional cylindrical and three-dimensional rectangular enclosures. Using

the P_N approximation, we can transform the radiative transfer equation into a set of simultaneous partial differential equations with high accuracy. This is also an advantage of P_N approximation. The disadvantage of the method is that complicated reformulation is required when we need to use a different order for approximation.

The discrete ordinates method has been used frequently in multidimensional radiative heat transfer problems. The discrete ordinate method was proposed by Chandrasekhar [17] to evaluate the intensities at 2n discrete directions instead of the two coordinate directions. The discrete ordinate method solves the radiative transfer equation for a set of discrete directions spanning the angle range from 0 to 4π. This method has two drawbacks, ray effect and false scattering. The impact of these drawbacks can be minimized by increasing the order of angular discretization and spatial grid [18]. We will discuss those effects in the next section. The discrete ordinate procedure has been used for solving the radiative heat transfer equation because of its small computational cost and accuracy, and compatibility with other computational fluid dynamics (CFD) methods.

Among the methods to solve the radiative heat transfer equation with participating media, the finite volume method proposed by Chui and Raithby [19] and Chai et al.[20] have been used in this study. The finite volume method is one of the popular methods used in CFD procedures and has been applied to many situations. The finite volume method has many similarities with the discrete ordinates method in sharing grid points and marching procedure. If this method is applied to a radiative heat transfer equation, the procedure is very efficient because the calculation procedure for a radiative

transfer equation can share the same grid point set for other dependent variables in the finite volume method. We can specify angular discretization in any manner, even in complex geometries [20], because the finite volume method calculates the value of $\int \hat{n} \cdot \hat{s} d\Omega$ instead of the angular weights used in the discrete ordinates method. Also, a finite volume method can be applied to multi-dimensional geometries without additional formulation procedures.

1.3 Ray Effect and False Scattering

If we use the discrete ordinates or finite volume method, it is important to understand the shortcomings of them.

One of the serious shortcomings of the discrete ordinates method is ray effect. This is a consequence of angular discretization. When we consider an enclosure with a very small volume (surface) with very high emission, intensity from this volume (surface) will be carried away from it into the discretized angular directions. Far away from the emission zone these intensities may become so far apart that some control volume (surface) can not receive any radiation energy from this high emission, and have zero intensity. This situation leads to physical unrealistic results and is called ray effect. The angular discretization practice causes ray effect and this effect is independent of the spatial discretization.

Another drawback is false scattering, which is a consequence of spatial discretization practice. It is also called false diffusion in computational fluid dynamics. This occurs when the direction of radiation is sloping with respect to the grid lines. This

physically unrealistic smearing of the radiative intensity is known as false scattering. It is independent of the angular discretization. Finer spatial grids can reduce false scattering, but the ray effect becomes more noticeable. Thus when using a finer spatial grid, a finer angular method is also needed [21].

1.4 Motivation and Objective

In most of the previous studies involving combined convection and radiation the effect of property variation resulting from radiative effects on the momentum field was not considered. In this study combined convection and radiation in a three-dimensional rectangular channel with and without a backward-facing step is considered. Variation of thermophysical properties (density, kinematic viscosity, and thermal conductivity) with temperature was considered in this study. Flow over a backward-facing step is considered as a standard benchmark problem due to rich flow physics that it entails, viz. flow separation, recirculation, and reattachment [22]. The other reason for its popularity as a benchmark problem is its simple geometry [23 and 24].

The objectives of this study are:

1. To develop a numerical code that can be used to simulate combined laminar forced convection and radiation heat transfer in a three-dimensional rectangular channel using a finite volume method.
2. To study the effect of combined forced convection and radiation on temperature field and reattachment length distribution in a three-dimensional rectangular channel with a horizontal backward-facing step.

3. To present the effect of variation of thermophysical properties with temperature on the velocity and temperature fields.
4. To study and compare the effects of radiative parameters such as optical thickness (τ_H=0.1, 0.2, and 0.4) and scattering albedo (ω=0, 0.25, 0.5, 0.75, and 1) on bulk temperature, Nusselt number, and reattachment length distribution along the channel for the cooling case.

1.5 Dissertation Outline

In this section the importance, literature review, motivations, and objectives for this study are stated. A literature review related to the topic of combined mode fluid flow and heat transfer problem in the two- and three-dimensional channel is presented. Also, a brief review about methods for solving a radiation heat transfer equation is also mentioned.

In Section 2, the geometry and assumption considered in this study are presented. These are followed by governing equations and boundary conditions to describe fluid flow and heat transfer. Radiative equation and its useful quantities are defined. Since the geometry in this study includes a horizontal backward-facing step, the treatments of irregular geometry (step) for numerical code are described.

Section 3 contains the solution technique including grid generation, discretization method, Semi-Implicit Method for Pressure Linked Equations (SIMPLE) algorithm, and Tri-Diagonal Matrix Algorithm (TDMA). The finite volume technique for solving the three-dimensional convective and radiative equations is included. Iteration sequence and

convergence criteria are also mentioned.

Section 4 shows the numerical validation and grid independence studies of the algorithm. The code is validated by comparing reattachment line distribution and temperature distribution with those of others. Study of combined convection and radiation in a channel without a backward facing step was treated as a part of validation. This study was published in 'International Journal for Computational Methods in Engineering Science and Mechanics'. A copy of this paper [25] is enclosed in Appendix A.

In section 5 numerical results are presented and discussed. The results include the effects of optical thickness (τ_H) and scattering albedo (ω) on bulk temperature, Nusselt number, and reattachment length distribution along the channel for the cooling case.

Section 6 includes a summary and conclusions of the numerical study discussed in previous sections.

2. PROBLEM FORMULATION

2.1 Geometry and Assumptions

A schematic of the system considered in the present study is shown in Figure 2.1. The step height (s) is assumed to be half of the channel height (H). The channel and backward-facing step have an aspect ratio $AR = W / s = 4$ and an expansion ratio $ER = H /(H - s) = 2$. The total length of the channel (L) is equal to 52 times the step height and the length of step (l) is 2 times the step height. The particular geometry considered here is identical to the one considered by Barbosa-Saldana et al. [26].

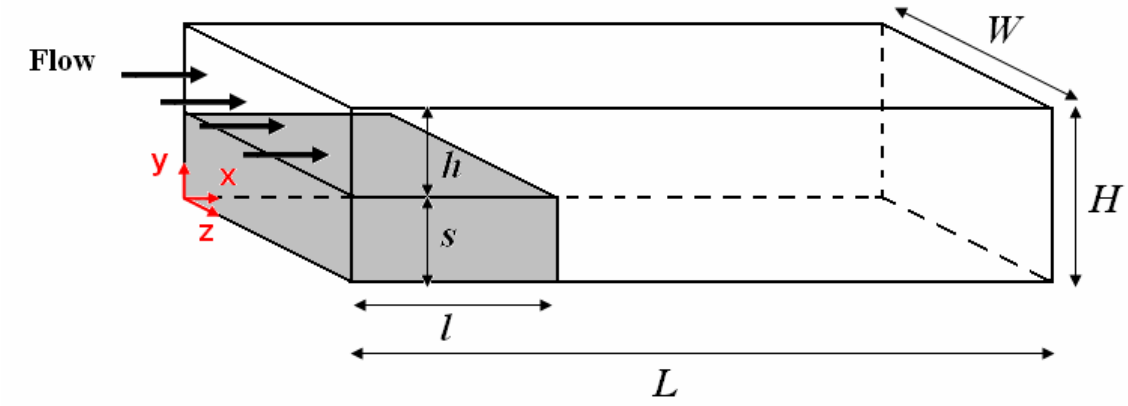

Figure 2.1. Schematic of the three-dimensional backward-facing step.

In this study the following simplifying assumptions were made for the development of the mathematical model:

1. Laminar flow
2. Steady state
3. Incompressible flow

4. Viscous dissipation terms were neglected
5. Thermophysical properties of fluid (air) are considered to vary with temperature
6. Gravitational forces are negligible
7. No internal heat generation
8. Flow medium is participating and gray

The variations of the thermophysical properties of the fluid with temperature were approximated by the piecewise-linear function of temperature as follows:

$$\phi(T) = \frac{\phi_{n+1} - \phi_n}{T_{n+1} - T_n}(T - T_n) + \phi_n \tag{2.1}$$

Thermophysical properties of gas with temperature 300*K* to 1,000*K* are shown in Table 2.1 below.

Table 2.1 Thermophysical properties of air at atmospheric pressure [27]

T (K)	ρ (kg/m^3)	C_P $(kJ/kg \cdot K)$	$\mu(10^7)$ $(N \cdot s/m^2)$	$\nu(10^6)$ (m^2/s)	$k(10^3)$ $(W/m \cdot K)$
300	1.1614	1.007	184.6	15.89	26.3
350	0.9950	1.009	208.2	20.92	30.0
400	0.8711	1.014	230.1	26.41	33.8
450	0.7740	1.021	250.7	32.39	37.3
500	0.6964	1.030	270.1	38.79	40.7
550	0.6329	1.040	288.4	45.57	43.9
600	0.5804	1.051	305.8	52.69	46.9
650	0.5356	1.063	322.5	60.21	49.7
700	0.4975	1.075	338.8	68.10	52.4
750	0.4643	1.087	354.6	76.37	54.9
800	0.4354	1.099	369.8	84.93	57.3
850	0.4097	1.110	384.3	93.80	59.6
900	0.3868	1.121	398.1	102.9	62.0
950	0.3666	1.131	411.3	112.2	64.3
1000	0.3482	1.141	424.4	121.9	66.7

2.2 Governing Equations

The fundamental governing equations of fluid flow and heat transfer are continuity, momentum, and energy equations. The governing equations for present study can be expressed in the Cartesian vector notation for steady, incompressible laminar flow as follows:

Continuity:

$$\nabla \cdot \rho \vec{V} = 0 \tag{2.2}$$

Momentum

$$\vec{V} \cdot \nabla \left(\rho \vec{V} \right) = -\nabla P + \nabla \cdot \mu \left(\nabla \vec{V} \right) \tag{2.3}$$

Energy

$$\vec{V} \cdot \nabla \left(\rho C_P T \right) = \nabla \cdot \left(k \nabla T \right) - \nabla \cdot q \tag{2.4}$$

Eq. (2.2) is also called the Navier-Stokes equation. Since variations of thermophysical properties of fluid with temperature are considered, the momentum equations are not independent of the energy equation. Thus the momentum and energy equations are coupled.

Note that the divergence of the radiative heat flux equation in the energy equation of Eq. (2.4) is used as a radiative source term and defined as follows:

$$\nabla \cdot q = \kappa \left(4\sigma_s T^4 - \int_{4\pi} I d\Omega \right) = \kappa (4\pi I_b - G) \tag{2.5}$$

where G is the incident radiation. If there is no heat source, sink, and other modes of heat transfer, Eq. (2.5) equals to zero and the system is called *radiative equilibrium* [28].

In radiative equilibrium the condition temperature of the medium can be obtained directly from Eq. (2.5).

2.3 Radiative Transfer Equation

The radiation intensity for an absorbing, emitting, and scattering gray medium at any position, $\vec{r}$, along a path, $\hat{s}$, is defined as [29]

$$\frac{dI(\vec{r},\hat{s})}{ds} = -\beta(\vec{r})I(\vec{r},\hat{s}) + S(\vec{r},\hat{s}) \tag{2.6}$$

where the extinction coefficient (β) and the source function (S) is written as

$$\beta(\vec{r}) = \kappa(\vec{r}) + \sigma(\vec{r}) \tag{2.7}$$

$$S(\vec{r},\hat{s}) = \kappa(\vec{r})I_b(\vec{r}) + \frac{\sigma(\vec{r})}{4\pi}\int_{4\pi} I(\vec{r},\hat{s}^l)\Phi(\hat{s}^l,\hat{s})\,d\Omega^l \tag{2.8}$$

The above equation indicates that the change of intensity along a path, or the energy accumulation, is equal to the difference between the energy gained and energy lost. The extinction coefficient represents attenuation of radiation intensity due to absorption and out-scattering. The source function means augmentation of intensity due to the gas emission and in-scattering.

The scattering phase function (Φ) describes how radiant energy is scattered by a participating medium and satisfies the following relation

$$\int_{4\pi} \Phi(\hat{s}^l,\hat{s})d\Omega^l = 4\pi \tag{2.9}$$

Scattering could be isotropic and anisotropic. Isotropic scattering means energy is scattered equally in all directions. Anisotropic scattering can be divided into forward and

backward scattering. Forward scattering scatters more energy in the forward directions, whereas backward scattering scatters more energy in the backward directions. The analytical expression for the scattering phase function is expressed by approximation using a finite series of Legendre polynomial as follows [5]:

$$\Phi^{ll'} = \Phi(\cos\Psi) = \sum_{j=0}^{K} C_j P_j(\cos\Psi) \tag{2.10}$$

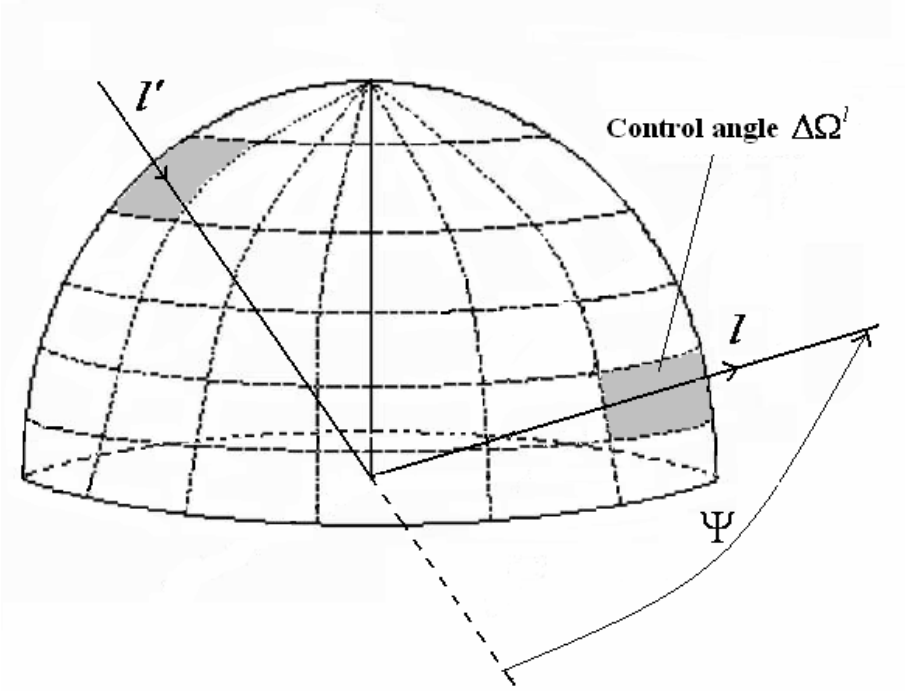

Figure 2.2. Scattering angle

where Ψ and C_j are the scattering angle between radiation direction l and l', and the phase function expansion coefficient respectively. Figure 2.2 showed the schematic scattering angle. The expansion coefficient depends on the size and reflective index of the particle. Table 2.2 shows the phase function series expansion coefficient [30].

Table 2.2 The phase function expansion coefficients [30]

j	F0	F1	F2	F3	F4	Isotropic	B1	B2
0	1.000	1.000	1.000	1.000	1.000	1.000	1.000	1.000
1	2.782	2.536	2.009	0.554	1.200		-0.565	-1.200
2	4.259	3.565	1.563	0.560	0.500		0.298	0.500
3	5.387	3.980	0.674	0.116			0.086	
4	6.190	4.002	0.222	0.011			0.010	
5	7.745	3.664	0.047	0.001			0.001	
6	7.067	3.016	0.007	0.000				
7	7.210	2.233	0.001					
8	7.201	1.303	0.000					
9	7.036	0.535						
10	6.766	0.201						
11	6.359	0.055						
12	5.834	0.011						
13	5.230							
14	4.479							
15	3.690							
16	2.816							
17	1.923							
18	1.115							
19	0.508							
20	0.209							
21	0.071							
22	0.021							
23	0.005							
24	0.001							
25	0.000							
26	0.000							
C1/3	0.927	0.845	0.670	0.185	4.000	0.000	-0.188	-0.400

The incident radiation (G) and radiative heat flux (q) are defined as

$$G(\vec{r}) = \int_{4\pi} I(\vec{r}, \hat{s}) d\Omega \tag{2.11}$$

$$q_x(\vec{r}) = \int I(\vec{r}, \hat{s})(\hat{s} \cdot n_x) d\Omega \tag{2.12}$$

$$q_y(\vec{r}) = \int I(\vec{r}, \hat{s})(\hat{s} \cdot n_y) d\Omega \tag{2.13}$$

$$q_z(\vec{r}) = \int I(\vec{r}, \hat{s})(\hat{s} \cdot n_z) d\Omega \tag{2.14}$$

2.4 Treatment of Horizontal Step

If the computational domains include irregular geometries, additional treatment is needed in the program code. In this study the temperature is given on a boundary (upper wall of step). Because this boundary is an internal domain in the computational procedure, we cannot specify the temperature on a boundary, directly.

The computational domain that includes the step region was assumed to have a very high value of conductivity and viscosity to have the same wall temperature and a zero velocity in the step region, respectively [31]. As a result, the temperature through the step region (high conductivity) will have the same value specified on the boundary.

To ensure the continuity of heat flux at the solid (step)-fluid interface, pseudo-solid-specific-heat method was used [32]. The block-off region procedure proposed by Chai et al. [33] was implemented to treat the radiative heat transfer of the step region. The significant temperature difference imposed between the inlet and the walls was considered for the radiation effects.

2.5 Boundary Conditions

A zero velocity condition was imposed at all y- and z- boundary walls. The velocity profile at the channel inlet was assumed as a fully developed flow [34]. The inlet bulk velocity U_0 was computed from Reynolds number, channel height H, and kinematic viscosity ν according to Eq. (2.15).

$$U_o = \frac{\mathrm{Re}\nu}{H} \tag{2.15}$$

We assumed a constant uniform wall and inlet temperature, *Tw* and *Tin*, respectively. The gradient of the transport variable (ϕ) in the flow direction is zero at the out flow.

We also need to mention the intensity boundary conditions to solve the radiative transfer equation. The boundary condition for an opaque diffuse wall given in the form of the boundary intensity case is expressed as

$$I(\vec{r},\hat{s}) = \varepsilon(\vec{r})I_b(\vec{r}) + \frac{\hat{\rho}(\vec{r})}{\pi}\int I(\vec{r},\hat{s}')\left|\hat{s}'\cdot\vec{n}\right|d\Omega' \tag{2.16}$$

The first term on the right-hand side of Eq. (2.16) represents the emission due to the surface temperature. The second term is the reflection of the incoming intensities at the wall. The inlet as well as outlet of the channel was assumed to be a pseudo-black wall.

In this work only cooling of the fluid flow was considered. In this case Tin and Tw were set at 1,000K and 300K respectively.

3. SOLUTION TECHNIQUE

3.1 Introduction

We have developed a numerical code that can handle governing equations including a radiative heat transfer equation in three-dimensional Cartesian coordinates. The spatial and angular domains were divided into a finite number of control volumes and control solid angles.

A finite volume method was used to solve flow fields along with the related boundary conditions. In this procedure, the momentum and energy equations inside the computational domain were discretized. The pressure and velocity fields were linked by the SIMPLE algorithm [35]. The solution to the one-dimensional convection diffusion equation was represented by the power law [35]. All scalar properties including pressure and temperature were located at the main grid nodes. But the modes for velocities were placed at staggered locations in each coordinate direction. At the outlet boundary, the condition of zero first-derivative was applied for all variables. The discretized equations for velocities, pressure, and temperature at each plane in the Cartesian coordinates were solved by the line-by-line method, which is a combination of the TDMA and the Gauss-Seidal procedure.

3.2 Staggered Grid

When we handle the governing equation, we need to consider the location of dependent variables to be calculated and stored in grids. Calculating the velocity

components and the pressure at the same grid point is the simplest and easiest way, but some physically unrealistic fields arise as solutions [35]. In order to avoid this kind of problem, the concept of the staggered grid was proposed by Harlow and Welch [36]. In the staggered grid, dependent variables are not all calculated at the same grid points. A two-dimensional staggered grid is used to illustrate the grid layout to avoid complex three-dimensional representation. Figure 3.1 illustrates the locations of the U velocity on the control volume faces in a three-dimensional geometry. The staggering for the V and W velocity component can be done in a similar way. All other variables, including pressure, and temperature, are calculated at the main grid points. This approach eliminates the possibility of unrealistic velocity distributions in the solution because each dependent variable can have a different grid if the volumes within each unique grid are not overlapped. In this approach, the center of velocity control volumes was located on the face of the temperature control volume.

One of the shortcomings of this staggered grid procedure is that dependent variables and properties should be interpolated between nodal values to give results at staggered nodes, which are located on the faces of the main central volumes.

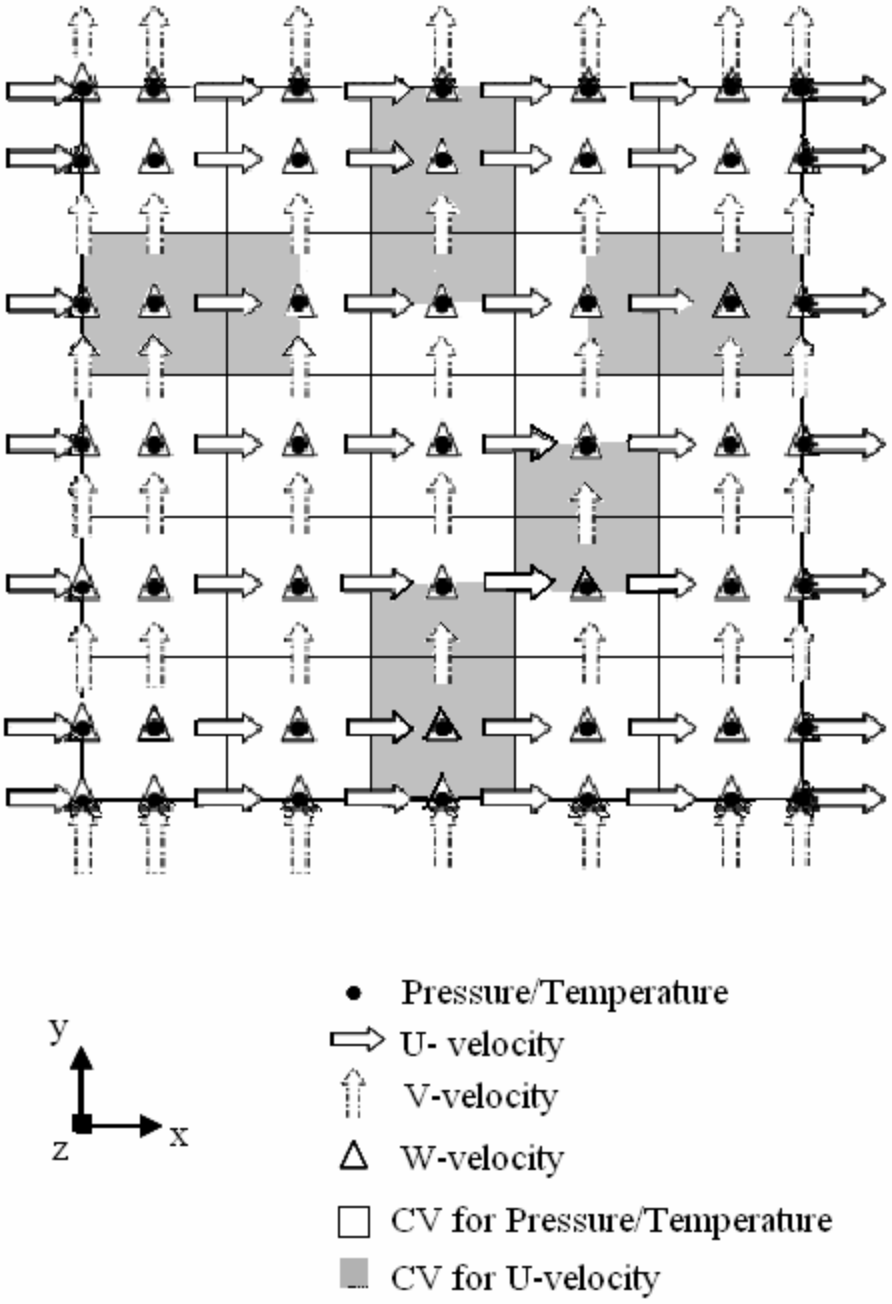

Figure 3.1. Staggered grid for U-velocity component at a constant z-plane

3.3 General Transport Equation

All conservation equations have similar structure. Thus a generalized equation of the governing equations can be applied to the flow and energy equations [37].

The generalized steady state transport equation for the variable ϕ can be written as

$$\nabla\left(\rho\phi\vec{V}\right)=\nabla\left(\Gamma_{\phi}\nabla\phi\right)+S_{\phi} \tag{3.1}$$

The left hand side of Eq. (3.1) represents the convection term, and the right hand side represents diffusion and source terms, respectively.

The transport equation can be identified by substituting the variables into Eq. (3.1). The values for the transport variables, diffusion coefficients and source terms for governing equations are given in Table 3.1.

Table 3.1. Values for the general transport equation

Transport variable (ϕ)	Diffusion coefficient (Γ_{ϕ})	Source term(S_{ϕ})	Equation
1	0	0	Mass Conservation
u	μ	$-\partial p/\partial x$	X-Momentum
v	μ	$-\partial p/\partial y$	Y-Momentum
w	μ	$-\partial p/\partial z$	Z-Momentum
T	k/C_p	Eq. (2.5)	Energy

3.4 Finite Volume Discretization

The finite volume technique presents considerable advantages because of its simplicity, easy numerical implementation, and applicability for dealing with complex geometries. The most significant characteristic is that the finite volume technique is conservative by construction; which means that for each finite control volume inside the computational domain the resulting discretized approximations for each property express an exact balance between the control volume and its neighbors [38]. In this research, the finite volume technique is applied to solve the momentum, energy, and radiative heat transfer equations.

The numerical solution domain is divided into a finite number of non-overlapping control volumes, and the conservation equations are applied to each control volume. At the center of each control volume lies a node point at which the variable values are to be calculated.

Figure 3.2 shows a schematic diagram of a control volume with dimensions Δx, Δy, and Δz. In Figure 3.2 the P is the nodal point and the N, S, W, E, T, and B represent the neighboring nodal points in each coordinate direction. The subscripts n, s, w, e, t, and b represent the face of the control volume at each coordinate direction. The variables δX, δY, and δZ are the distances (diffusion lengths) between the central point and the neighboring points according to the coordinate direction.

The numerical discretization implies that the transport equation for the variable ϕ would be expressed as an algebraic equation for each control volume inside the domain that involves the values of the physical quantity at the control volume and its neighbors.

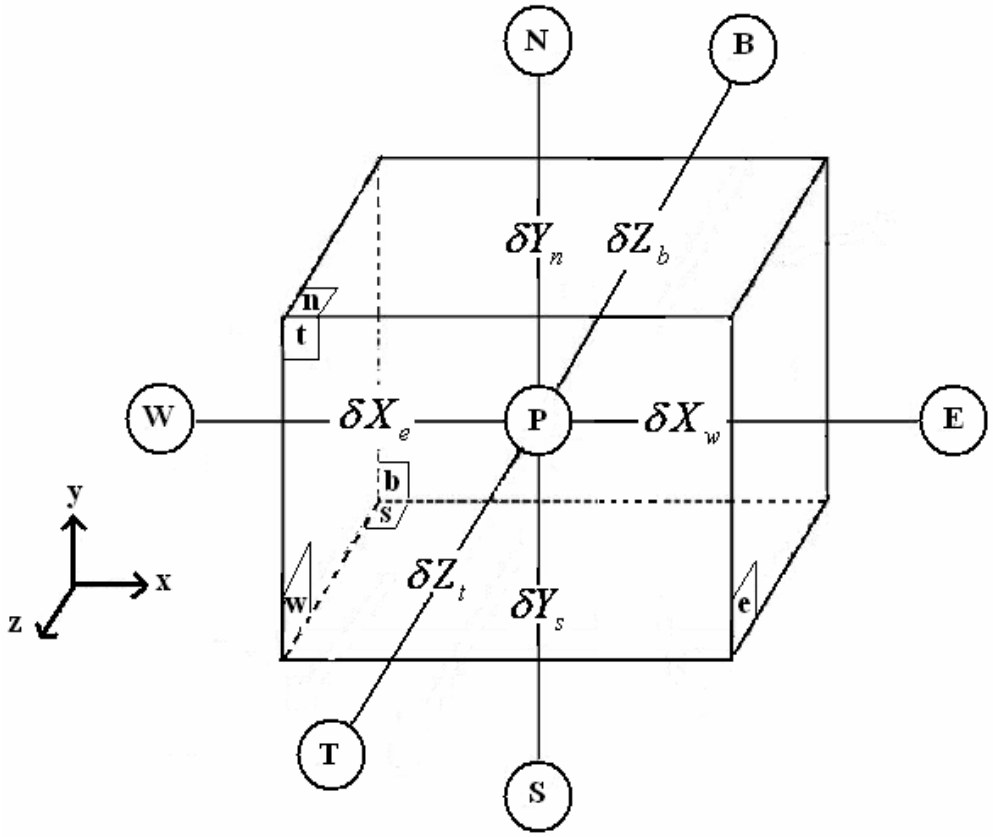

Figure 3.2. Control volume element with neighboring nodal points

A finite volume technique involves an integration of the transport equation for each control volume in the computational domain as follows:

$$\int_{cv} \nabla\left(\rho\phi\vec{V}\right)dv = \int_{cv} \nabla\left(\Gamma_\phi \nabla\phi\right)dv + \int_{cv} S_\phi dv \tag{3.2}$$

The discretized form of the governing equation can be obtained after integration followed by applying the divergence theorem in Eq. (3.2)

The discretized governing equation becomes

$$\left(\rho u\phi-\Gamma_\phi\frac{\partial\phi}{\partial x}\right)_e dydz-\left(\rho u\phi-\Gamma_\phi\frac{\partial\phi}{\partial x}\right)_w dydz$$
$$+\left(\rho v\phi-\Gamma_\phi\frac{\partial\phi}{\partial y}\right)_s dxdz-\left(\rho v\phi-\Gamma_\phi\frac{\partial\phi}{\partial y}\right)_n dxdz \qquad (3.3)$$
$$+\left(\rho w\phi-\Gamma_\phi\frac{\partial\phi}{\partial z}\right)_t dxdy-\left(\rho w\phi-\Gamma_\phi\frac{\partial\phi}{\partial z}\right)_b dxdy=\left(\bar{S}_\phi\right)dxdydz$$

As shown in Eq. (3.3), a combined convective and diffusive flux must be known at the control volume faces. The fluxes are defined at the control volume surfaces in each direction, but they need to be expressed with the value of the neighboring nodal points. In order to find an appropriate approximation to evaluate the convection-diffusion flux at the face of the control volume several methods have been developed, such as central difference, upwind, exponential, hybrid, and power law schemes. Patankar developed the so-called power law scheme [35], which is an approximation of the exact solution of the one-dimensional convection-diffusion behavior for the property ϕ. The Power Law scheme is represented by the equation below;

$$A(|P|)=\max\left|0,\left(1-0.1|P|\right)^5\right| \qquad (3.4)$$

where P (cell Peclet number) is the ratio of flow to diffusion variables as

$$P_i=F_i/D_i \qquad (3.5)$$

$$F_i=\left(\rho u_i\right)\Delta A \qquad (3.6)$$

$$D_i=\left(\frac{\Gamma_\phi}{\delta x_i}\right)\Delta A \qquad (3.7)$$

Note that the value of Γ_ϕ is evaluated using the harmonic mean of properties in the neighboring nodal points.

The discretized transport equation in three-dimensions is represented as follows:

$$a_P \phi_p = \sum_{i=1}^{n} a_i \phi_i + \bar{S}_\phi \Delta x \Delta y \Delta z \tag{3.8}$$

where

$$a_E = D_e A\left(\left|P_e\right|\right) + [\![-F_e, 0]\!] \tag{3.9}$$

$$a_W = D_w A\left(\left|P_w\right|\right) + [\![F_w, 0]\!] \tag{3.10}$$

$$a_N = D_n A\left(\left|P_n\right|\right) + [\![-F_n, 0]\!] \tag{3.11}$$

$$a_S = D_s A\left(\left|P_s\right|\right) + [\![F_s, 0]\!] \tag{3.12}$$

$$a_T = D_t A\left(\left|P_t\right|\right) + [\![-F_t, 0]\!] \tag{3.13}$$

$$a_B = D_b A\left(\left|P_b\right|\right) + [\![F_b, 0]\!] \tag{3.14}$$

$$a_P = a_E + a_W + a_N + a_S + a_T + a_B \tag{3.15}$$

In Eq. (3.8) the sub index "*P*" refers to the nodal point and the "*n*" should be interpreted as the number of neighbors surrounding 6 nodal points in a three dimensional problem. The operator $[\![a, b]\!]$ is equivalent to max [a,b] and returns the larger one between two numbers.

Note that the radiative source term in the energy equation is the function of temperature. In such case this dependence could result in numerical instabilities, which precludes reaching a convergent solution. Thus, we must express this dependence in a linear form to avoid the numerical instabilities by following method [35]

$$\overline{S}_{\phi} = S_c + S_P T_P = S^* + \left(\frac{dS}{dT}\right)^* (T_P - T_P^*) \tag{3.16}$$

where the asterisk symbol was used to represent the previous value of the marked variables. Only negative values of S_P are allowed to facilitate a diagonal dominance condition that ensures at least one solution to the linear system of equations [35].

Considering the source term linearization, the discretized transport equation in three-dimensions is written below.

$$a_P \phi_p = \sum_{i=1}^{n} a_i \phi_i + b \tag{3.17}$$

where

$$b = S_c \Delta x \Delta y \Delta z \tag{3.18}$$

$$a_P = a_E + a_W + a_N + a_S + a_T + a_B - S_P \Delta x \Delta y \Delta z \tag{3.19}$$

The coefficients of other nodal points are not changed.

From this final form for the general transport equation we can solve the continuity, momentum, and energy equations. We need to solve the radiative equation to find the source term in the energy equation. Thus the next step is the solution procedure for the radiative transport equation.

3.5 Finite Volume Discretization of Radiative Transfer Equation

Since radiative intensities have to be solved in the spatial and angular domains, the discretization procedure of Eq. (2.6) should include these two discretizations. To discretize Eq. (2.6) the finite volume method was used. The finite volume method for

radiative heat transfer has formulated the discretization by integration over the spatial control volume and angular control angle. The control angles used in this study are the solid angles proposed by Chui et al. [39], and a typical control angle is shown in Figure 3.3. The angular space is subdivided into $N_\theta \times N_\varphi = M$ control angles.

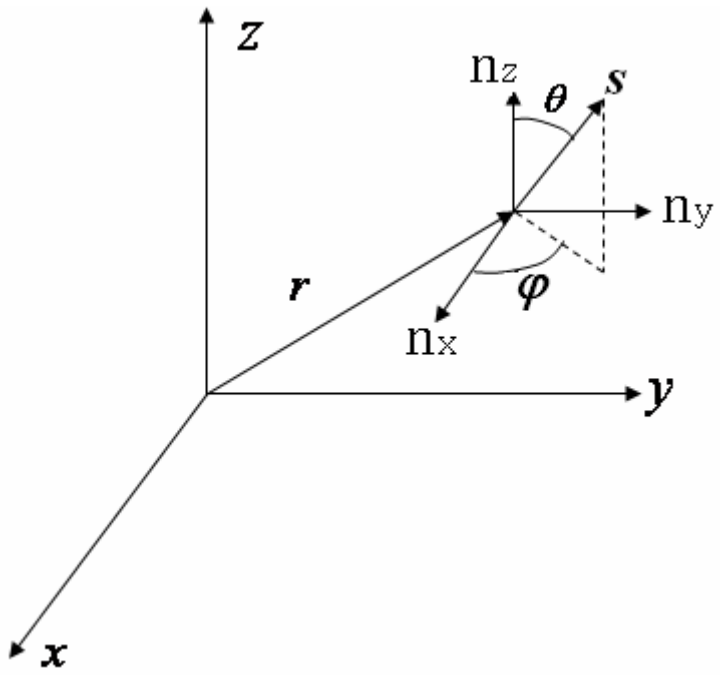

Figure 3.3. A typical angular direction.

Integrating Eq. (2.6) over a control angle and control volume can be written as

$$\int_{\Delta\Omega^l}\int_{\Delta v} I^l(\hat{s}^l \cdot \vec{n})dv\,d\Omega^l = \int_{\Delta\Omega^l}\int_{\Delta v}(-\beta I^l + S^l)dv\,d\Omega^l \tag{3.20}$$

Applying the divergence theorem in Eq. (3.20) gives

$$\int_{\Delta\Omega^l}\int_{\Delta A} I^l(\hat{s}^l \cdot \vec{n})dA\,d\Omega^l = \int_{\Delta\Omega^l}\int_{\Delta v}(-\beta I^l + S^l)dv\,d\Omega^l \tag{3.21}$$

In the control volume approach, the intensity within a control volume is assumed to be constant. With this assumption, Eq. (3.21) can be simplified to

$$\sum_{i=1}^{6} I_i^l \Delta A_i \int_{\Delta\Omega^l} (\hat{s}^l \cdot \vec{n}_i) d\Omega^l = (-\beta I^l + S^l) \Delta v \, \Delta\Omega^l \tag{3.22}$$

$$S^l = \kappa I_b + \frac{\sigma}{4\pi} \sum_{l'=1}^{M} I^{l'} \bar{\Phi}^{l'l} \Delta\Omega^{l'} \tag{3.23}$$

The left hand side of Eq. (3.22) represents the inflow and outflow of radiative energy across the six control volume faces, and the right hand side represents the attenuation and augmentation of radiative energy within a control volume. Note that in Eq. (3.22) the magnitude of the intensity is assumed constant, but the radiation direction varies within a control angle. In Eq. (3.23) $\bar{\Phi}^{l'l}$ is the average scattering phase function from control angle l to l'. In the finite volume method, the phase function in Eq. (2.9) can be expressed as

$$\int_{4\pi} \Phi(\hat{s}^l, \hat{s}) d\Omega^l = \sum_{l'=1}^{M} \bar{\Phi}^{l'l} \Delta\Omega^{l'} \tag{3.24}$$

Chui et al. [39] proposed the approach to evaluate the average scattering phase function as follows:

Using the source term linearization of Patankar [35], the modified extinction coefficient and the modified source function can be expressed as [20]

$$\beta_m^l = (\kappa + \sigma) - \frac{\sigma}{4\pi} \Phi^{ll} \Delta\Omega^l \tag{3.25}$$

$$S_m^l = \kappa I_b + \frac{\sigma}{4\pi} \sum_{l'=1, l' \neq l}^{M} \Phi^{l'l} I^{l'} \Delta\Omega^{l'} \tag{3.26}$$

With these expressions, Eq. (3.22) becomes

$$\sum_{i=1}^{6} I_i^l \Delta A_i \int_{\Delta\Omega^l} (\hat{s}^l \cdot \vec{n}_i) d\Omega^l = (-\beta_m I^l + S_m^l) \Delta v \, \Delta\Omega^l \tag{3.27}$$

From Eq. (2.16) the discretized boundary condition for an opaque diffuse wall is expressed as

$$I_w = \varepsilon_w I_B + \frac{\rho_w}{\pi} \sum_{D_{cx}^{l'}} I_w^{l'} D_{cx}^{l'} \tag{3.28}$$

To relate the intensity at the boundaries of control volumes to the nodal intensities, a spatial differencing scheme is needed. The diamond scheme was used in the present study and the final discretized equation could be expressed as follows [40]:

$$a_P^l I_P^l = a_W^l I_W^l + a_E^l I_E^l + a_S^l I_S^l + a_N^l I_N^l + a_B^l I_B^l + a_T^l I_T^l \tag{3.29}$$

where

$$a_W^l = \max\left(\Delta A_e D_{ce}^l - \Delta A_w D_{cw}^l, 0\right) \tag{3.30}$$

$$a_E^l = \max\left(\Delta A_w D_{cw}^l - \Delta A_e D_{ce}^l, 0\right) \tag{3.31}$$

$$a_S^l = \max\left(\Delta A_n D_{cn}^l - \Delta A_s D_{cs}^l, 0\right) \tag{3.32}$$

$$a_N^l = \max\left(\Delta A_s D_{cs}^l - \Delta A_n D_{cn}^l, 0\right) \tag{3.33}$$

$$a_B^l = \max\left(\Delta A_t D_{ct}^l - \Delta A_b D_{cb}^l, 0\right) \tag{3.34}$$

$$a_T^l = \max\left(\Delta A_b D_{cb}^l - \Delta A_t D_{ct}^l, 0\right) \tag{3.35}$$

$$\begin{aligned} a_P^l = {} & \max\left(2\Delta A_e D_{ce}^l, 0\right) + \max\left(2\Delta A_w D_{cw}^l, 0\right) + \max\left(2\Delta A_e D_{ce}^l, 0\right) \\ & + \max\left(2\Delta A_w D_{cw}^l, 0\right) + \beta_P \Delta V_P \Delta\Omega^l \end{aligned} \tag{3.36}$$

$$b^l = S_P \Delta V_P \Delta\Omega^l \tag{3.37}$$

$$D_{ce}^l = -D_{cw}^l = \int (s^l \cdot n_x) d\Omega^l \tag{3.38}$$

$$D_{cn}^{l} = -D_{cs}^{l} = \int (s^{l} \cdot n_{y}) d\Omega^{l} \tag{3.39}$$

$$D_{ct}^{l} = -D_{cb}^{l} = \int (s^{l} \cdot n_{z}) d\Omega^{l} \tag{3.40}$$

A typical angular direction is defined by the polar angle (θ) and the azimuthal angle (φ), and is expressed as

$$s = (\sin\theta\cos\phi)\vec{i} + (\sin\theta\sin\phi)\vec{j} + \cos\theta\vec{k} \tag{3.41}$$

This discretization of the radiative heat transfer equation resulted in a set of algebraic equations of intensity. The process of intensity calculation was repeated for all specified intensity directions. The detailed procedure is written below [30].

1. Guess an intensity field.
2. March in one direction, $D_{cx}^{l} > 0$, $D_{cy}^{l} > 0$, and $D_{cz}^{l} > 0$

   (a) Calculate the boundary intensity from Eq. (3.28).

   (b) Solve for the nodal intensity using Eq. (3.29).

   (c) Repeat steps 2(a) and 2(b) for all $D_{cx}^{l} > 0$, $D_{cy}^{l} > 0$, and $D_{cz}^{l} > 0$ directions.

3. Repeat Step 2 for $D_{cx}^{l} > 0$, $D_{cy}^{l} > 0$, and $D_{cz}^{l} < 0$ directions.
4. Repeat Step 2 for $D_{cx}^{l} > 0$, $D_{cy}^{l} < 0$, and $D_{cz}^{l} > 0$ directions.
5. Repeat Step 2 for $D_{cx}^{l} > 0$, $D_{cy}^{l} < 0$, and $D_{cz}^{l} < 0$ directions.
6. Repeat Step 2 for $D_{cx}^{l} < 0$, $D_{cy}^{l} > 0$, and $D_{cz}^{l} > 0$ directions.
7. Repeat Step 2 for $D_{cx}^{l} < 0$, $D_{cy}^{l} > 0$, and $D_{cz}^{l} < 0$ directions.

8. Repeat Step 2 for $D_{cx}^{l} < 0$, $D_{cy}^{l} < 0$, and $D_{cz}^{l} > 0$ directions.

9. Repeat Step 2 for $D_{cx}^{l} < 0$, $D_{cy}^{l} < 0$, and $D_{cz}^{l} < 0$ directions.

10. Repeat the cycle, from Step 2 to 9, with the previous iteration field until the solutions satisfy the convergence criteria.

3.6 SIMPLE Algorithm

The general calculation procedure is based on the solution of the general transport equation. However, the momentum equations require a separate treatment because of the staggered grid and existence of the pressure term. The pressure-correction and pressure equations should be included in the overall procedure. The particular treatment of these equations used in this study is called SIMPLE procedure. The SIMPLE algorithm stands for Semi-Implicit Method For Pressure-Linked Equations.

The calculation procedure of SIMPLE algorithm is outlined as follows [35]:

1. Start with the guessed value for the pressure field p*.
2. Using the guessed pressure distribution in step 1, calculate the coefficient in the momentum equations and obtain u*, v* and w*.
3. Solve the pressure correction p'. The pressure correction is obtained by integrating the continuity equation for each control volume using the velocity values computed in step 2. If the pressure distribution is equal to zero, then no further pressure correction is needed.
4. Update the pressure field by the addition of the guessed pressure p* to the pressure correction p', as follows:

$$p = p' + p^* \tag{3.42}$$

5. Update the new value *u, v,* and *w* from their guessed values using the velocity correction formula as follows:

$$u_e = u_e^* + \frac{A_e}{a_p^u}\left(P_P' - P_E'\right) \tag{3.43}$$

$$v_n = v_n^* + \frac{A_n}{a_p^v}\left(P_P' - P_N'\right) \tag{3.44}$$

$$w_t = w_t^* + \frac{A_t}{a_p^w}\left(P_P' - P_T'\right) \tag{3.45}$$

6. Replace guessed pressure (p') with new updated pressure field (Eq. 3.42). Return to step 2 and repeat procedure until pressure and velocity fields converge.

7. Solve the discretized equations for the other scalar variables (i.e. temperature).

3.7 Tri-Diagonal Matrix Algorithm (TDMA)

There are two categories for solving the discretized equation: direct methods and iterative method. The iterative method has an advantage of accuracy and memory storage, but needs many iterations for convergence.

When the discretized equations associated with the nodes in any particular plane are being solved, the currently available values of the dependent variables at the nodes on neighboring planes are treated as known values. To solve the discretized equation in the plane of interest a line-by-line TDMA is used. The TDMA [41] procedure is repeated plane-by-plane until the entire computational domain is swept. During the solution

process variables in other dimensions are treated as known values, and variables along each line are updated.

In this study, a three-dimensional computational domain is swept as follows:

1. For x-direction TDMA solving, sweep from south to north and from bottom to top.
2. For y-direction TDMA solving, sweep from west to east and from bottom to top.
3. For z-direction TDMA solving, sweep from south to north and from west to east.

Many sweeps of the computational domain in alternating directions are needed to obtain a converged solution.

3.8 Numerical Procedure and Convergence Criteria

The appropriate under-relaxation factors are imposed to avoid instability in the solution. Relaxation factor for velocity components, pressure, and temperature fields were set at 0.7, 0.4, and 0.6, respectively.

The numerical computing order for one iteration cycle is as follows. First, the momentum equation was solved to obtain velocities. After the velocity and pressure fields were obtained, the radiative heat transfer equation was solved to get the intensity and the divergence of radiative heat flux, which were used as a source term in the energy equation. When the maximum relative change of the radiative intensities fell below 10^{-6}, the intensities were stored as the initial values of the radiative heat transfer equation for

the next iteration, and the radiative heat flux was calculated. After we obtained the temperature distribution from the energy equation, all thermophysical properties were updated. This procedure was repeated until the convergence criteria were satisfied. The convergence criteria for velocity components and pressure are defined as follows [42]:

$$R_U = \frac{\sum_{nodes} \left| a_e U_e - \sum a_{nb} U_{nb} - A_e (P_P - P_E) \right|}{a_e U_e} \le \varepsilon_u \tag{3.46}$$

$$R_V = \frac{\sum_{nodes} \left| a_n V_n - \sum a_{nb} V_{nb} - A_n (P_P - P_N) \right|}{a_n V_n} \le \varepsilon_v \tag{3.47}$$

$$R_W = \frac{\sum_{nodes} \left| a_t W_t - \sum a_{nb} W_{nb} - A_t (P_P - P_T) \right|}{a_t W_t} \le \varepsilon_w \tag{3.48}$$

$$R_P = \frac{\rho \sum_{nodes} \left| (U_w - U_e) dydz + (V_s - V_n) dxdz + (W_b - W_t) dxdy \right|}{\rho U_{in} LH} \le \varepsilon_p \tag{3.49}$$

The convergence tolerance in this study was set to less than 1×10^{-6} for velocity, pressure, and temperature fields. For the temperature field, the convergence criteria required that the maximum relative change of each value between successive iterations be less than 1×10^{-6}.

4. VALIDATION AND GRID INDEPENDENCE

4.1 Numerical Validation

The numerical code was validated by reproducing results for three different problems: the friction factor and Nusselt number in rectangular ducts for pure forced convection, the temperature distributions in a rectangular enclosure filled with a participating medium, and *Xu*-line adjacent to backward-facing step for pure forced convective flow. In addition, to benchmark this code a three-dimensional combined convection and radiation in a rectangular channel without no steps was studied.

4.1.1 Forced Convective Flow through a Square Horizontal Channel

The first validation test was to study fully developed fluid flow in a rectangular duct. Shah and London [34] compiled data of flow and heat transfer for various cases. The friction factor and Nusselt number for a rectangular duct were used for validating this code. In the present 3-D code the source term in the energy equation (Eq. 2.4), was set to zero so that the temperature field could be compared with the ones by Shah and London [34] for fully developed flow in a straight channel of arbitrary length. The product of friction factor *f* and Re for fully developed laminar flow through a square channel is 57.048. The peripheral average local Nusselt number for constant wall temperature case was calculated using the following definition for a straight channel:

$$Nu_{p,x} = \frac{D_h \left(\left(\frac{\partial T}{\partial n} \right)_w \right)_x}{T_w - T_b} \tag{4.1}$$

The parameters given by Shah and London [34] are compared with those calculated by current numerical code and are given in Table 4.1. Comparisons presented in Table 4.1 lend credibility to our numerical predictions for flow and temperature fields without considering radiative heat transfer.

Table 4.1. Comparison of f Re and Nu for fully developed flow in a square channel

Parameters	Shah and London [34]	Present numerical model	Percent difference
f Re	56.908	57.048	0.246
Nu	3.091	3.0945	0.129

4.1.2 Radiative Trasnsfer in a Rectangular Enclosure

The second validation test was that for simulating a pure radiative heat transfer in a three-dimensional rectangular enclosure duct with participating medium. For the purpose of the code validation with radiative heat transfer part, the present results were compared with those obtained by Menguc and Viskanta [15]. This proposed test case consisted of a rectangular enclosure ($2m \times 2m \times 4m$) which was filled with an absorbing and emitting medium with $\beta = 0.5m^{-1}$. A uniform volumetric heat source of $q_g = 5kW/m^3$ was considered in the medium. The boundary conditions are given in Table 4.2.

Table 4.2. Boundary condition of rectangular enclosure [15]

Boundary	Temperature (K)	Wall emissivity (ε_w)
z=0	1200	0.85
z=4m	400	0.70
all other walls	900	0.70

The simulated temperature distributions for the test case are shown in Figure. 4.1. Computations were performed on $25\times25\times25$ uniformly sized control volumes and 8×24 control angles. Calculated temperature distributions in three different z-planes are in agreement with those obtained by Menguc and Viskanta [15] using P_3-approximation and by Chai et al. [20] using a finite volume method.

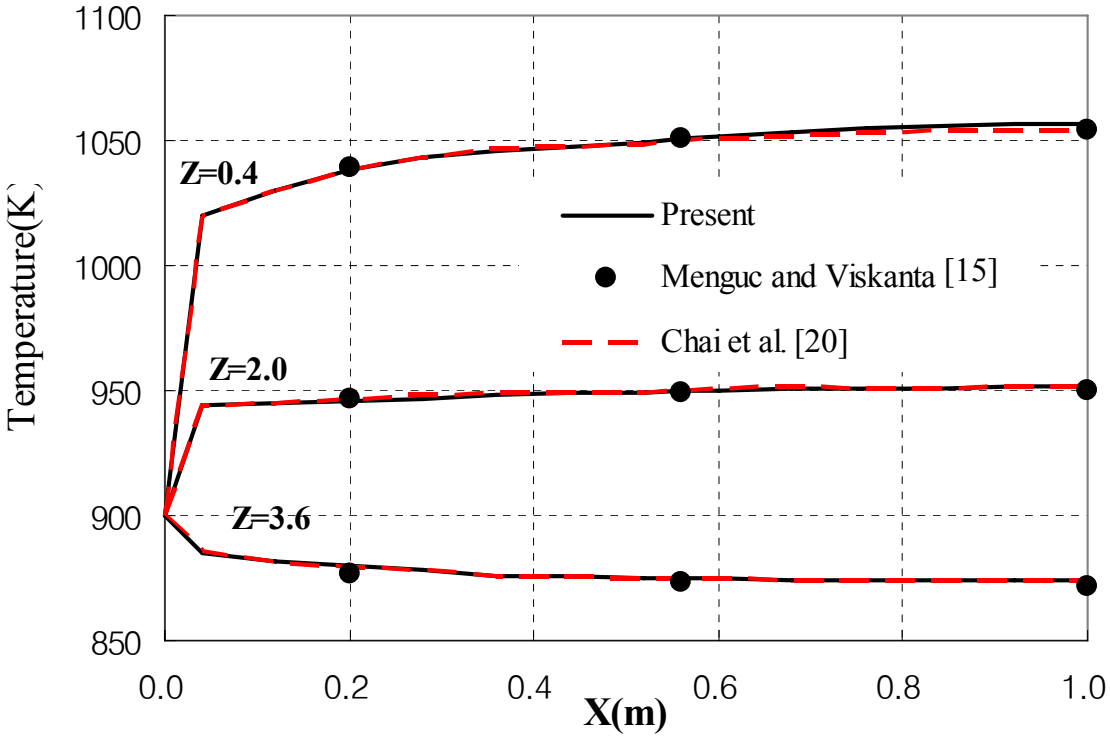

Figure 4.1. Temperature distribution at y=1m

4.1.3 Forced Convective Flow over a Three-Dimensional Horizontal Backward-Facing Step

The third validation test was that pure forced convective flow over a three-dimensional horizontal backward-facing step. Loci of all points of reattachment are called *Xu*-line. The primary vortex reattachment length (*Xu*-line) adjacent to the backward-facing step for pure forced convective flow was compared with those of Nie and Armaly [43]. They set the geometry as follows: a duct aspect ratio AR=8, an expansion ratio ER=2, and a step length equal to two times the step height. The numerical predictions using the present code were compared with the result for the same geometry. The *Xu*-line along the span-wise direction was used for validating the code. These distributions are presented in Figures 4.2 for Re=200 and 400. Flow at the inlet was considered to be fully developed and isothermal. The Reynolds number was defined based on the channel height and the bulk velocity at the channel inlet. The uniform grid used for this simulation was similar to the one used by Nie and Armaly in their numerical solution for this test problem. In the present numerical simulation a total of 3.36×10^5 nodal points were distributed in 140x40x60 control volumes along the x, y, and z directions, respectively. z/(W/2)=0 and 1 represents the wall and the central plane respectively. Because the reattachment lines showed a symmetric behavior with respect to the central plane (z/(W/2)=1), we presented the graph on half of the channel along the bottom wall. It was seen that the numerical results compared well with those presented by Nie and Armaly [43].

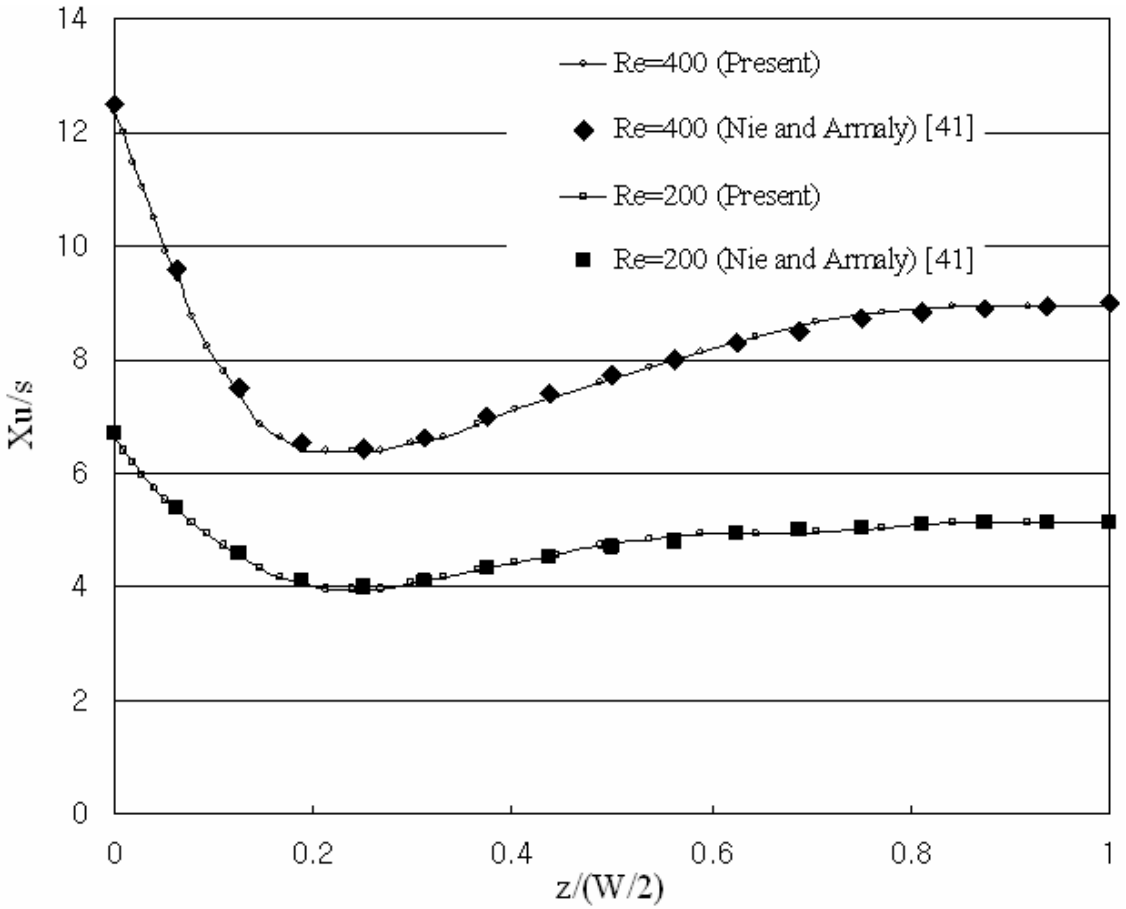

Figure 4.2. *Xu*-line (Re=200 and 400)

Based on the above results, it was concluded that the developed numerical code is an accurate one and could be reliably applied to study heat transfer and fluid flow over a three-dimensional backward-facing step problem under consideration.

4.1.4 Combined Convective Radiative Flow through a Three-Dimensional Horizontal Channel

The last validation test was that for simulating the combined convective radiative flow through a three-dimensional horizontal channel without a step. The effects of

Reynolds number, conduction-radiation parameters, absorption coefficient, and scattering albedo on the Nusselt number and bulk temperature profiles along the channel were predicted. This study was published in '*International Journal for Computational Methods in Engineering Science and Mechanics*'. In the interest of brevity a copy of this paper [25] is enclosed in Appendix A.

4.2 Grid Set-up

The geometry considered in this study is shown in Figure 2.1. Because the step and the fluid flow region have different thermophysical properties, the computational domain presents discontinuities. To handle these discontinuities the computational domain is divided such that the control volume faces coincide with the location of the discontinuities as well as the physical boundaries.

The grids were non-uniformly distributed and concentrated close to the step and corners in order to assure the accuracy of the numerical simulation using the grid expansion factor. The grid expansion ratio and grid positions are expressed by the following relation:

$$\delta_i(n) = \frac{L_i\left(e^n - 1\right)}{\left(e^N - 1\right)} \tag{4.2}$$

where $\delta_i(n)$ represents the distance from the wall to the face of the n^{th} control volume, L_i is the geometrical length that needs to be divided into the N total number of control volumes, and the e represents the grid expansion coefficient. Note that e=1 means that the grids are uniform.

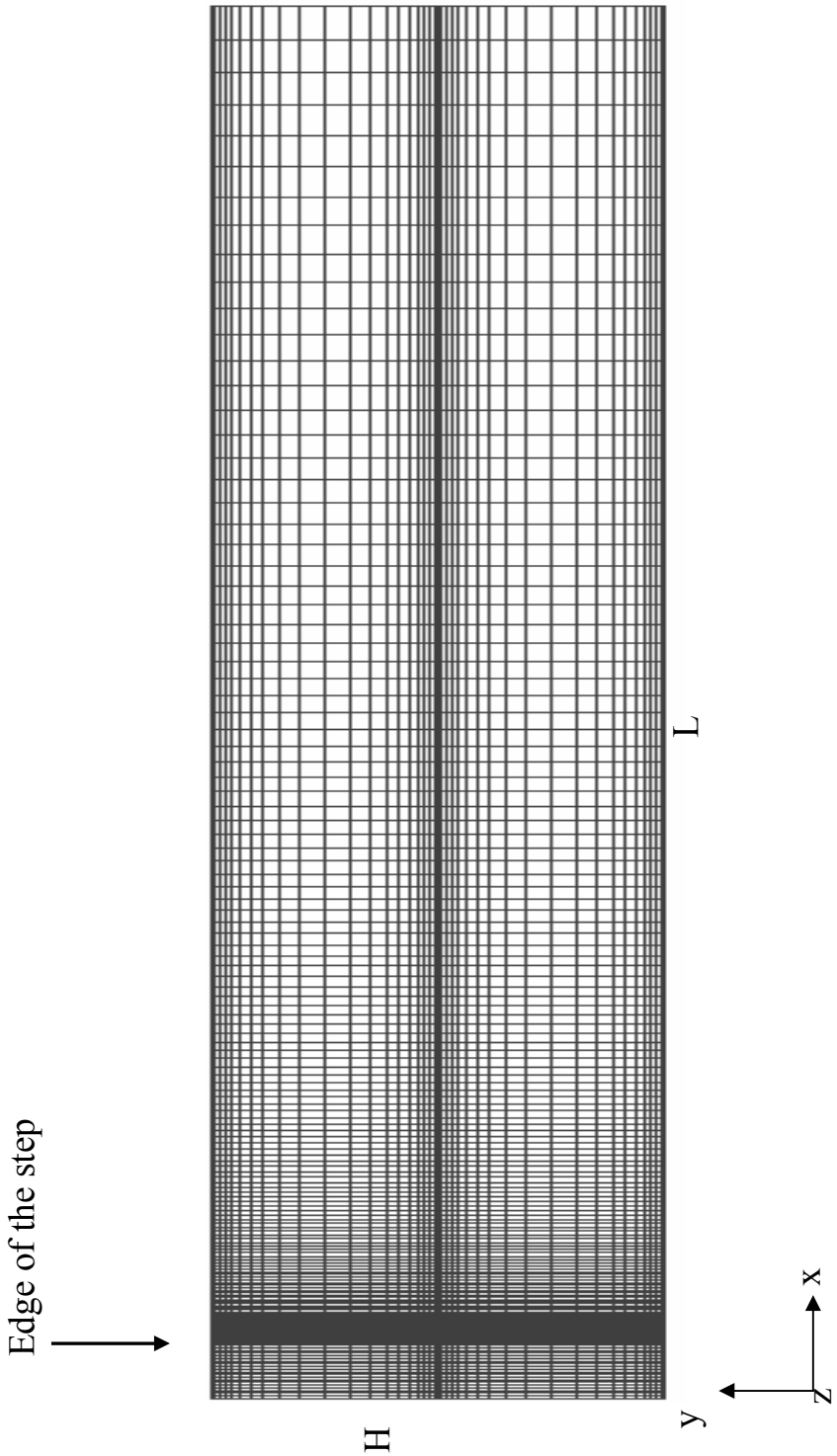

Figure 4.3. Non-uniform grid set-up in a constant z-plane

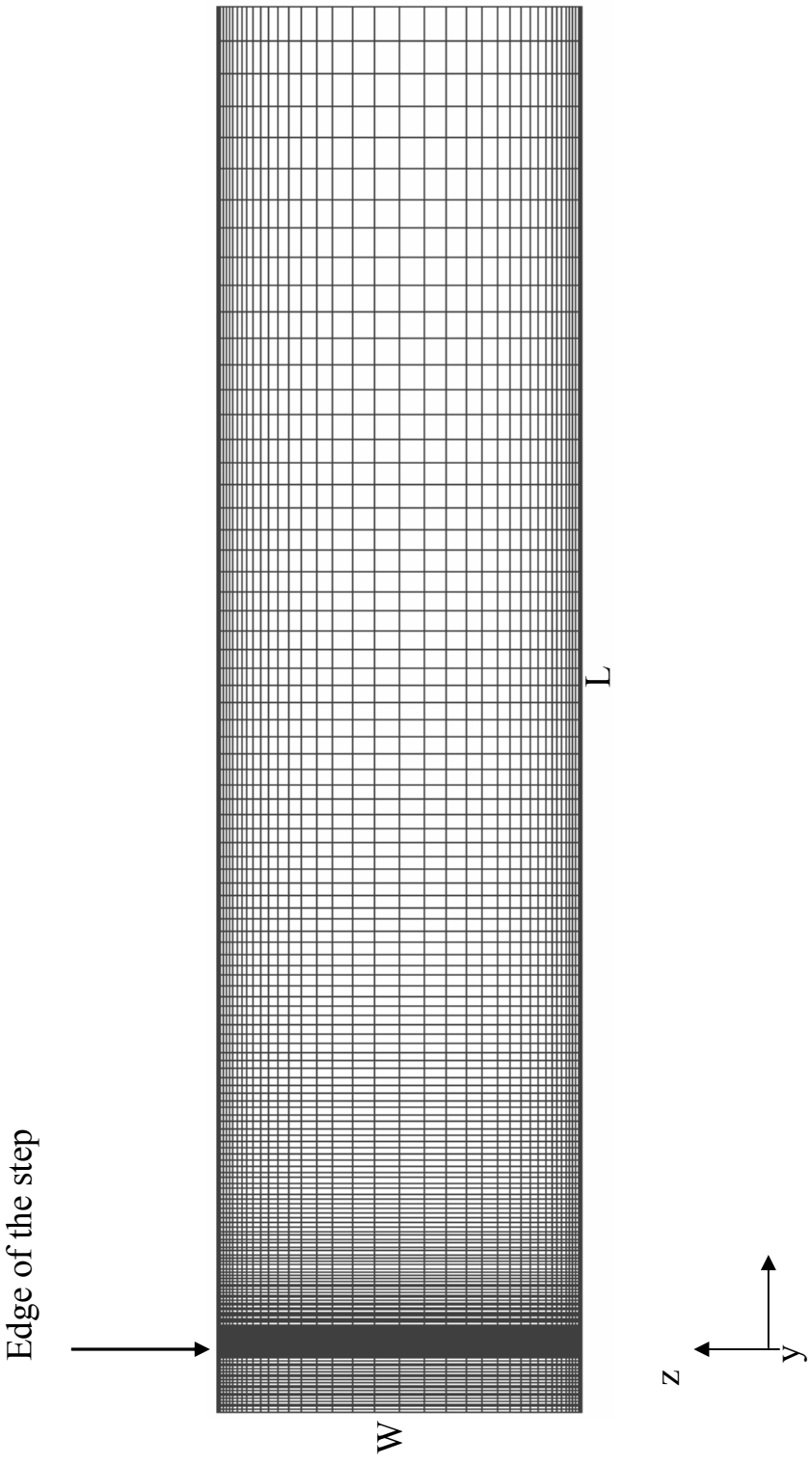

Figure 4.4. Non-uniform grid set-up in a constant y-plane

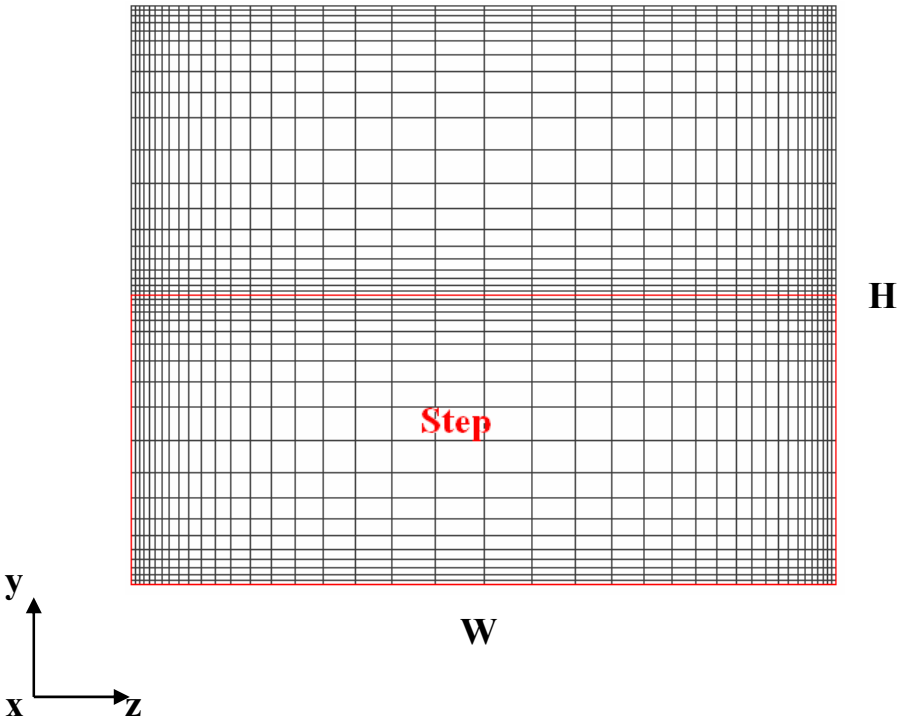

Figure 4.5. Non-uniform grid set-up in a constant x-plane

The x-direction is the largest dimension in the computational domain because it is the stream-wise flow direction. The backward-facing step length (l) represents a small portion of the total length in the x-direction. Also, the velocity gradients in this zone are negligible because we treated the inlet flow as hydrodynamically fully developed It is also expected that the velocity gradient is large near the downstream of the backward-facing step. For the above reasons, the region upstream of the backward-facing step was fitted with a uniform grid. The grid for the rest of the channel in the stream-wise direction was non-uniform with expansion ratio of 1.025.

In z-direction the smallest control volume is located at the side walls (z=0 and W), then the grid is spread to the central plane (z=W/2) with expansion ratio of 1.15.

In y-direction we need to consider the solid region and the flow inlet region. A symmetry line was considered at half of the channel in the y-coordinate direction. Thus, the smallest control volume is located near y=0, H/2, and H. The grid is expanded to the middle of solid region (z=H/4) and the middle of the flow inlet height (z=3H/4) with expansion ratio of 1.15.

To give a better understanding of the grid set-up in this geometry, each plane is shown in Figures 4.3 - 4.5.

4.3 Grid Independence Study

Grid independence of the solution was tested with several grid density changes in x-direction for $\mathrm{Re} = 200, \kappa = 20, \tau_H = 0.4, T_w = 300K,$ and $T_{in} = 1,000K.$ We used expansion ratios of 1.025:1.15:1.25 for x, y, and z directions, respectively. The Nusselt number at the outlet was monitored to declare grid independence (Table 4.3). The difference in the results of the span-wise averaged total Nusselt number at the channel exit obtained using a $(N_x \times N_y \times N_z) = (160 \times 40 \times 40)$ and $(180 \times 40 \times 40)$ was less than 2%. Accordingly, we chose $160 \times 40 \times 40$ non-uniformly spaced grids in this study to make parametric runs.

Table 4.3. Grid independence study - span-wise averaged total Nusselt number at the channel outlet

Grid size	Total number of cells	Percent difference in number of cells	Nu	Percent difference in Nu
$120\times40\times40$	192000		4.9868	
$140\times40\times40$	224000	16.67	4.7925	3.896
$160\times40\times40$	256000	14.29	4.7175	1.565
$180\times40\times40$	288000	12.5	4.6835	0.721

5. RESULTS AND DISCUSSION

5.1 Parameters and Definitions

The optical thickness represents the total strength of absorption and scattering. The optical thickness is one of the parameters affecting radiative energy transfer, and is defined as

$$\tau = (\kappa + \sigma)H \tag{5.1}$$

The relative ratio of absorption and scattering can be described using scattering albedo as follows:

$$\omega = \frac{\sigma}{\kappa + \sigma} \tag{5.2}$$

Once the velocity, radiative intensity, and temperature fields are converged, the bulk temperatures along the channel were calculated using the following equation:

$$T_b = \frac{\iint \rho C_p |u| T dy dz}{\iint \rho C_p |u| dy dz} \tag{5.3}$$

We also have interest in the thermal entry length. Thus we define the bulk mean temperature as:

$$\theta_b = \frac{T_b - T_w}{T_{in} - T_w} \tag{5.4}$$

The definitions for the averaged span-wise convective (Nu_c), radiative (Nu_r), and total Nusselt numbers (Nu_t) are given as follows:

$$Nu_c = \frac{H\left(d\overline{T}/dy\right)\Big|_{y=0}}{\left(T_b - T_w\right)} \tag{5.5}$$

$$Nu_r = \frac{H \cdot q_r\,|_{y=0}}{k\left(T_b - T_w\right)} \tag{5.6}$$

$$Nu_t = Nu_c + Nu_r \tag{5.7}$$

where q_r in Eq. (5.6) is radiative heat fluxes and is calculated by the summation of q from Eqs. (2.12)-(2.14).

Also, the reattachment length (*Xu)* was studied. This reattachment length is the location along the bottom wall adjacent to the step where the shear stress ($\mu \partial u / \partial y\,|_{y=0}$) is equal to zero. Loci of all points along the bottom wall wherein the wall shear stress is zero is termed as *Xu*-line.

5.2 Effect of Optical Thickness

The optical thickness of a medium is a well-known radiation property that affects the temperature distribution. Figure 5.1 illustrates the effect of the optical thickness (τ_H=0.1, 0.2, and 0.4) on the bulk mean temperature and *Xu*-line distribution for the non-scattering medium with *Re* = 200, $T_w = 300K$, and $T_{in} = 1,000K$. A higher value of τ_H means that the medium's ability to absorb and emit energy is greater. The bulk mean temperature for the pure forced convection case was also presented to compare the effects of radiation heat transfer. From this comparison, we can easily understand that the thermal development is augmented by radiation effect. For the case of τ_H=0.1

compared to τ_H=0.4, the bulk mean temperature gradually decreases from inlet to outlet (Figure 5.1(a)). It is evident from Figure 5.1(a) that the bulk temperature decreases with an increase in optical thickness. Also, the drop in bulk temperature is much steeper at higher values of optical thickness. As expected, the fluid participates in the radiation transfer process by absorbing more energy radiated from the wall and emitting more energy to the medium at higher optical thickness values. Hence, the medium approaches the wall temperature at a much shorter distance from the entrance at higher optical thickness values.

Figure 5.1(b) shows the *Xu*-line distribution. In the vicinity of the side walls the highest (x-*l*)/s values for the *Xu*-line are found for all cases. This behavior can be explained by the no slip condition imposed on the side wall. Also, the minimum values are located approximately at z/(W/2)=0.5. This behavior is due to the influence of the viscous effects and the no slip condition imposed on the side walls. Note that the kinematic viscosity of the fluid decreases from $121.9\times10^{-6} m^2/s$ to $15.89\times10^{-6} m^2/s$ in the temperature range of 1,000K to 300K. Figures 5.2 and 5.3 represent the variations of density and viscosity distributions for each case, respectively. In the temperature change from 1,000K to 300K the kinematic viscosity decreases by a factor of 7.6 and the density increases by a factor of 3.34. If we apply mass conservation to inlet and outlet, then the outlet bulk velocity can be calculated approximately as:

$$U_{out} = \frac{\rho_{in} A_{in}}{\rho_{out} A_{out}} U_{in} = \frac{1}{(3.335)(2)} U_{in} = 0.15 U_{in} \tag{5.8}$$

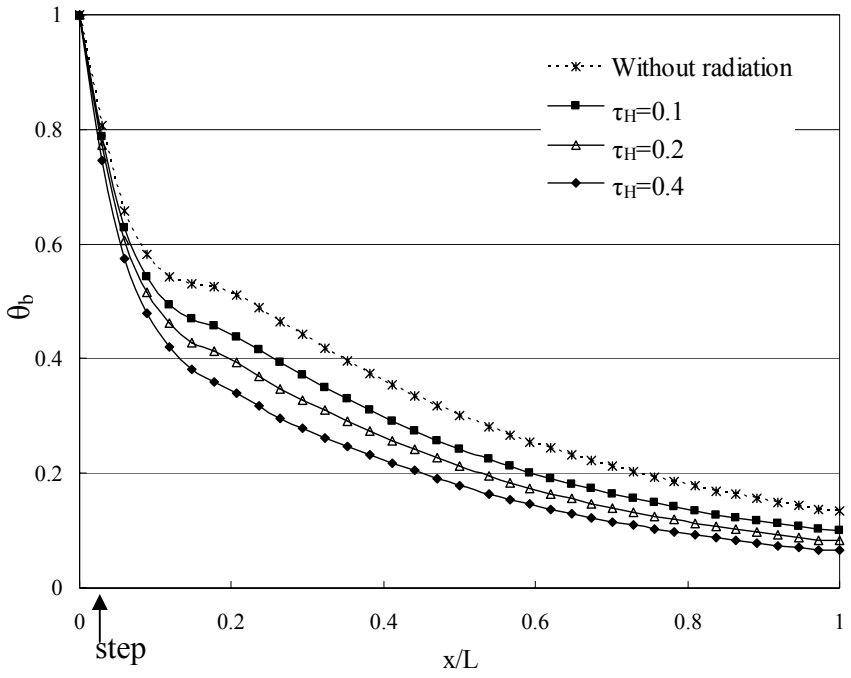

(a)

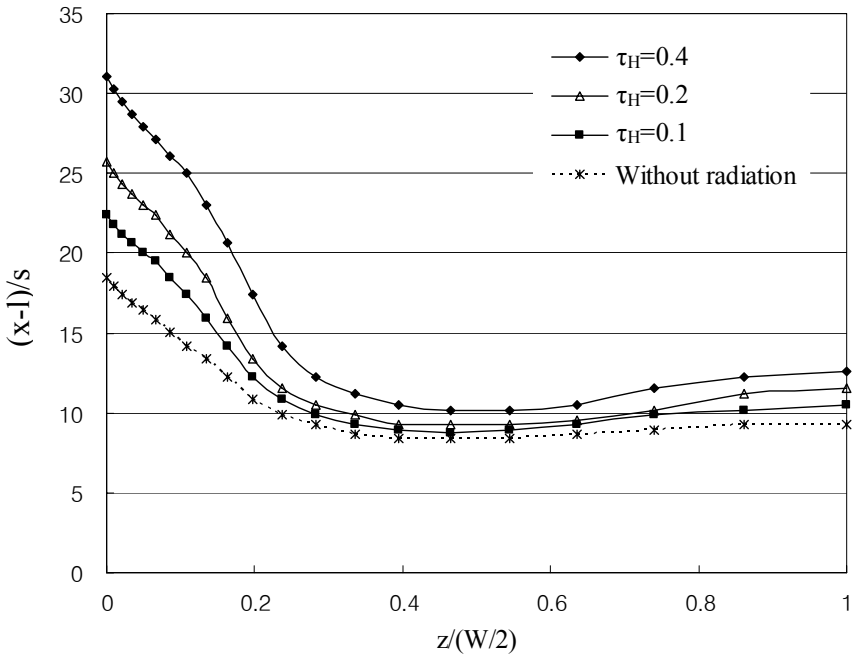

(b)

Figure 5.1. Effect of optical thickness:
(a) bulk mean temperature; (b) *Xu*-line distribution

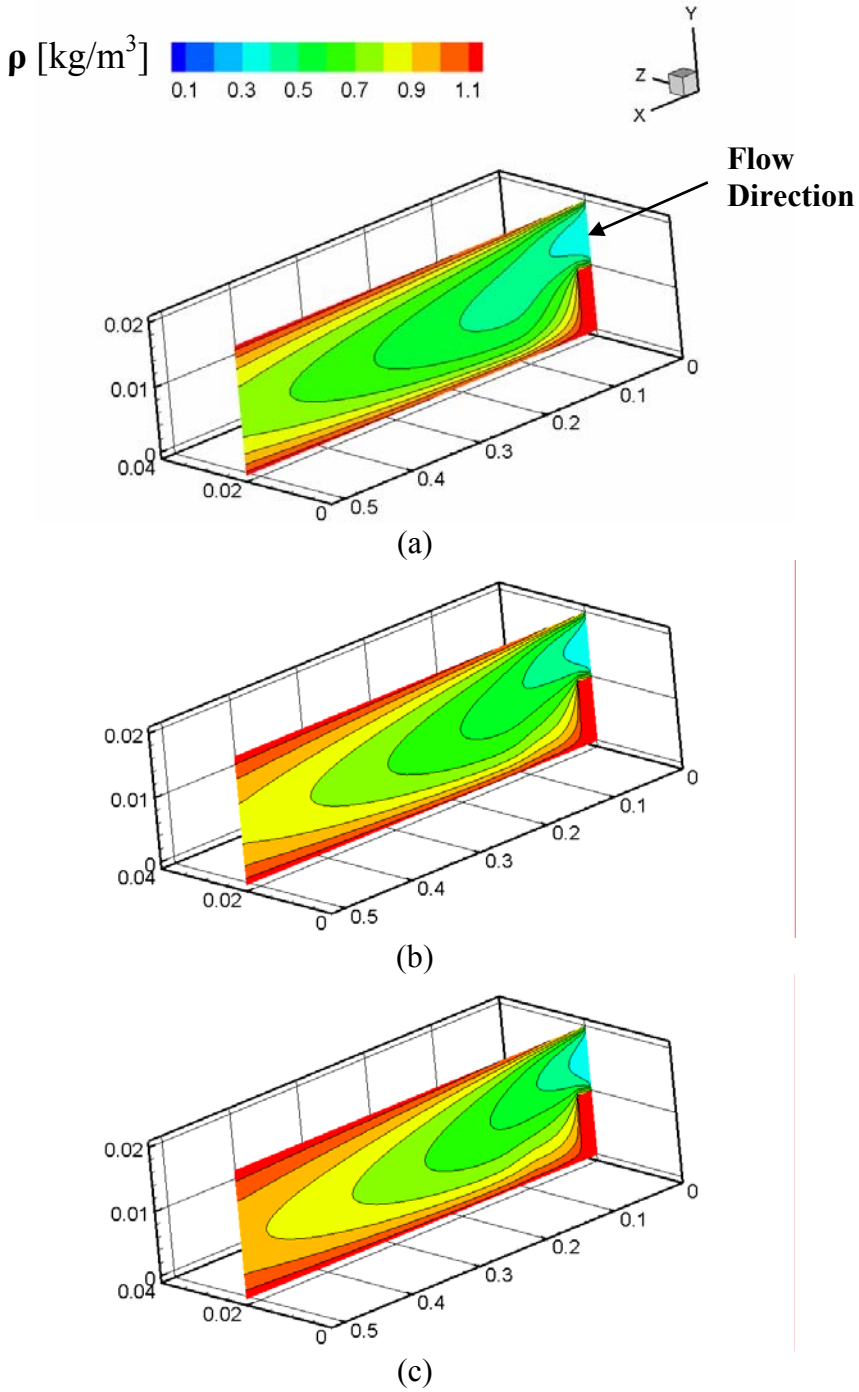

Figure 5.2. Density distributions at constant z-plane (z=0.02): (a) forced convection; (b)τ_H=0.2; (c)τ_H=0.4

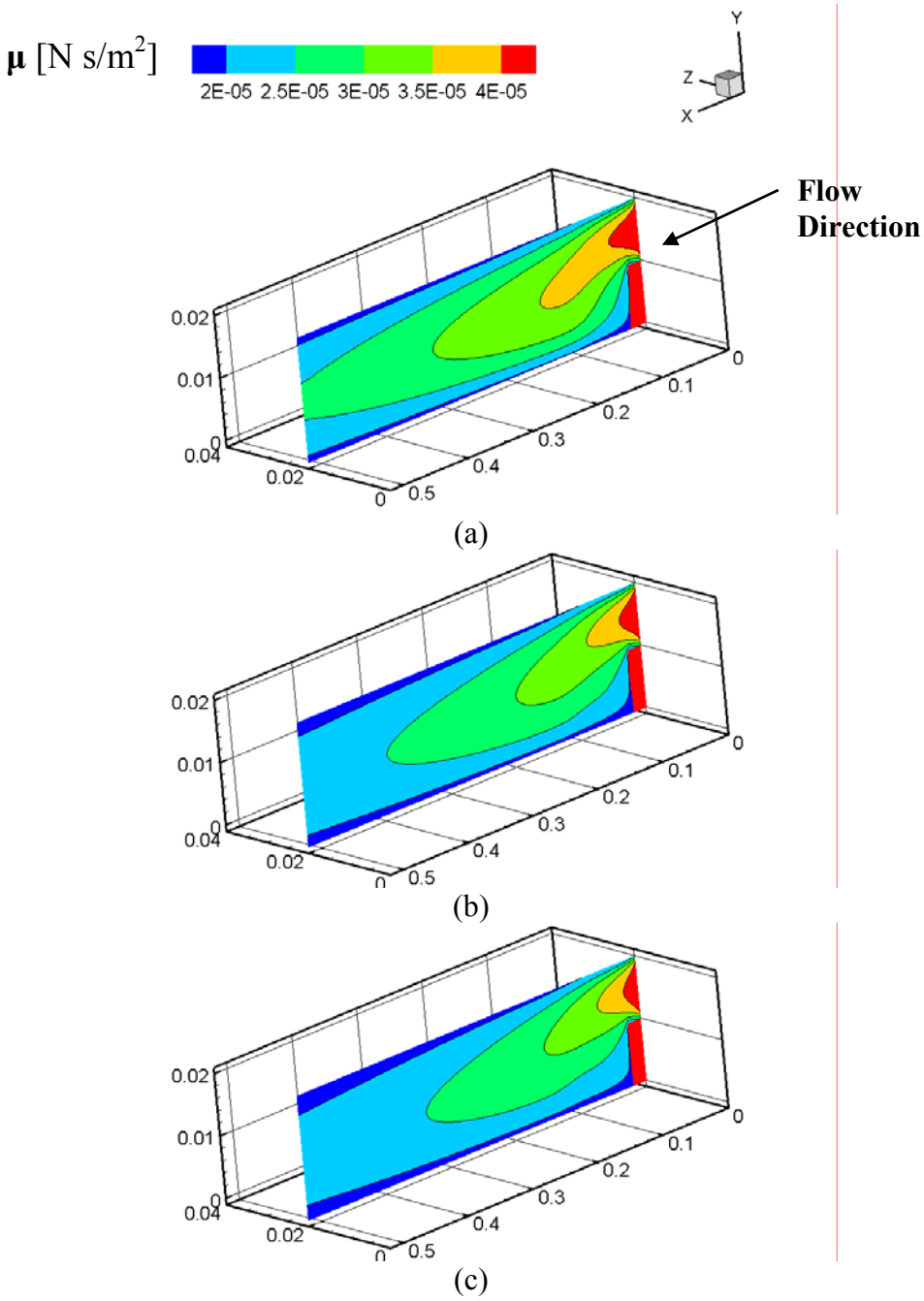

Figure 5.3. Viscosity distributions at constant z-plane (z=0.02): (a) forced convection; (b)τ_H=0.2; (c)τ_H=0.4

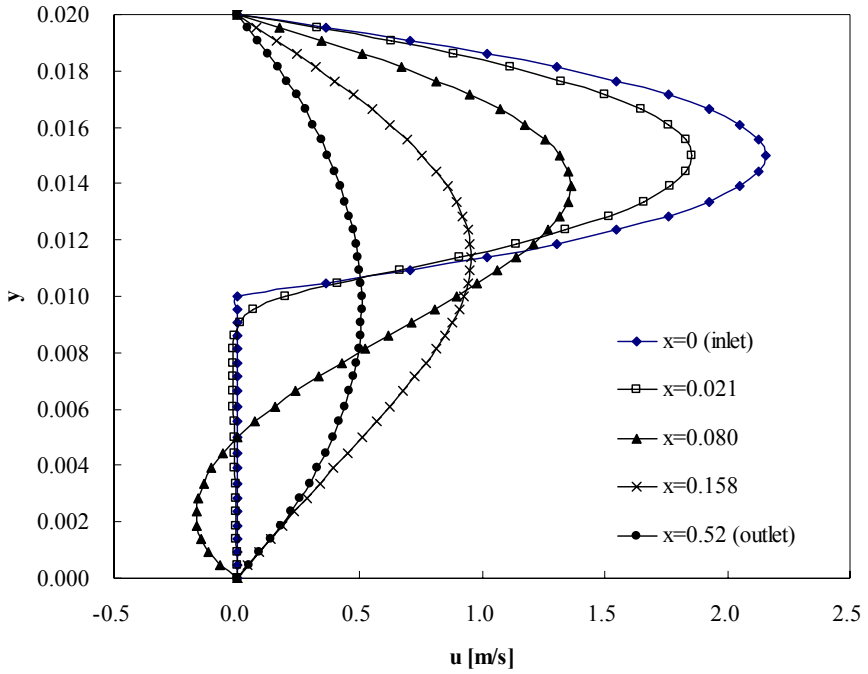

(a)

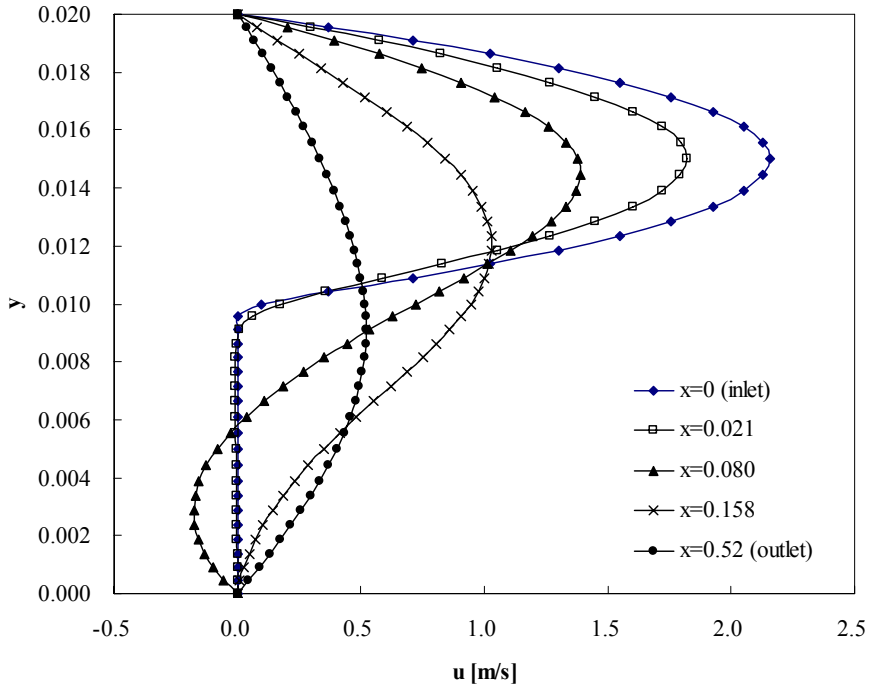

(b)

Figure 5.4. U-velocity profile at plane z=0.02 at different x positions: (a) forced convection; (b) τ_H=0.4

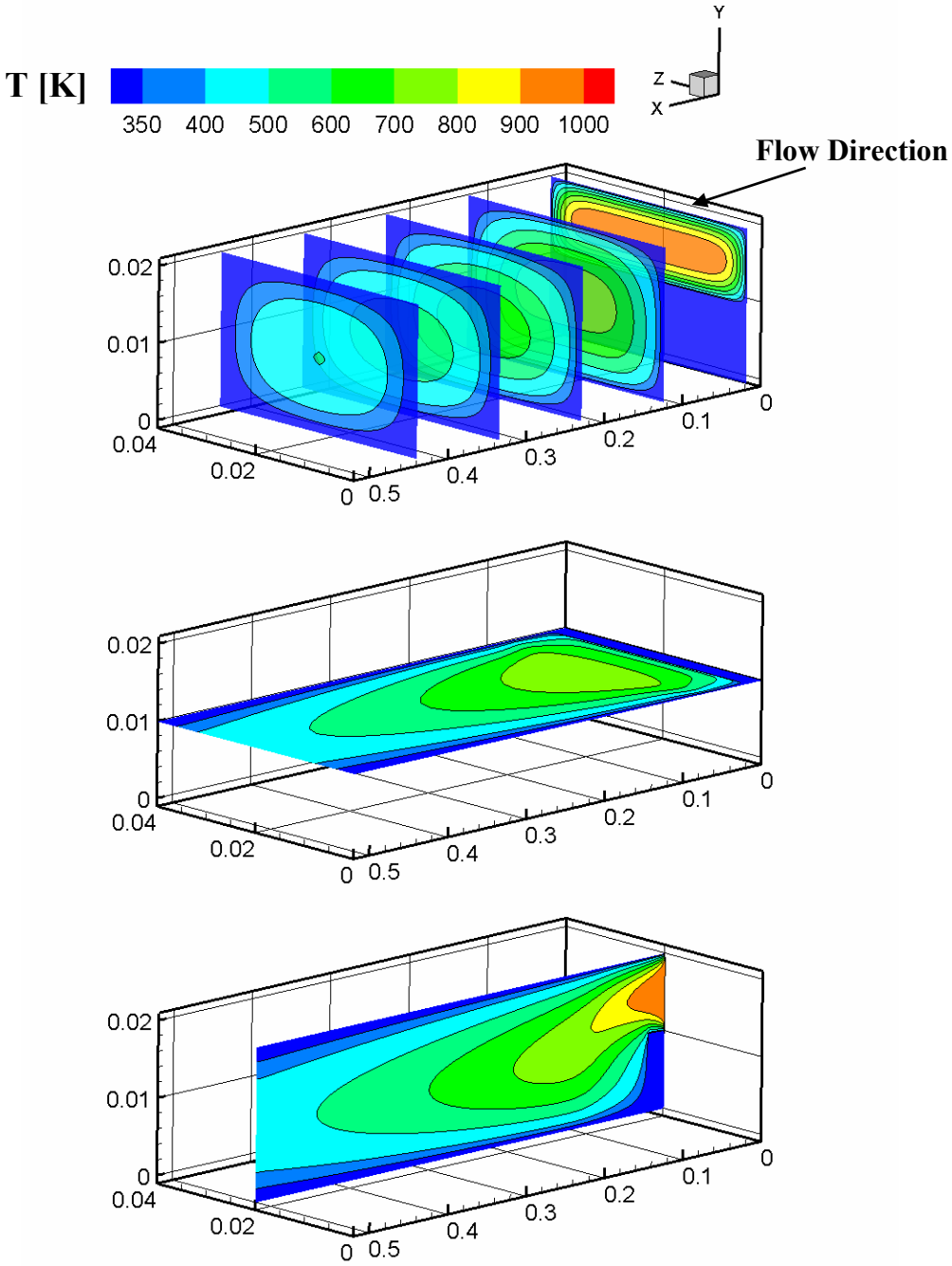

Figure 5.5. Temperature distributions for forced convection

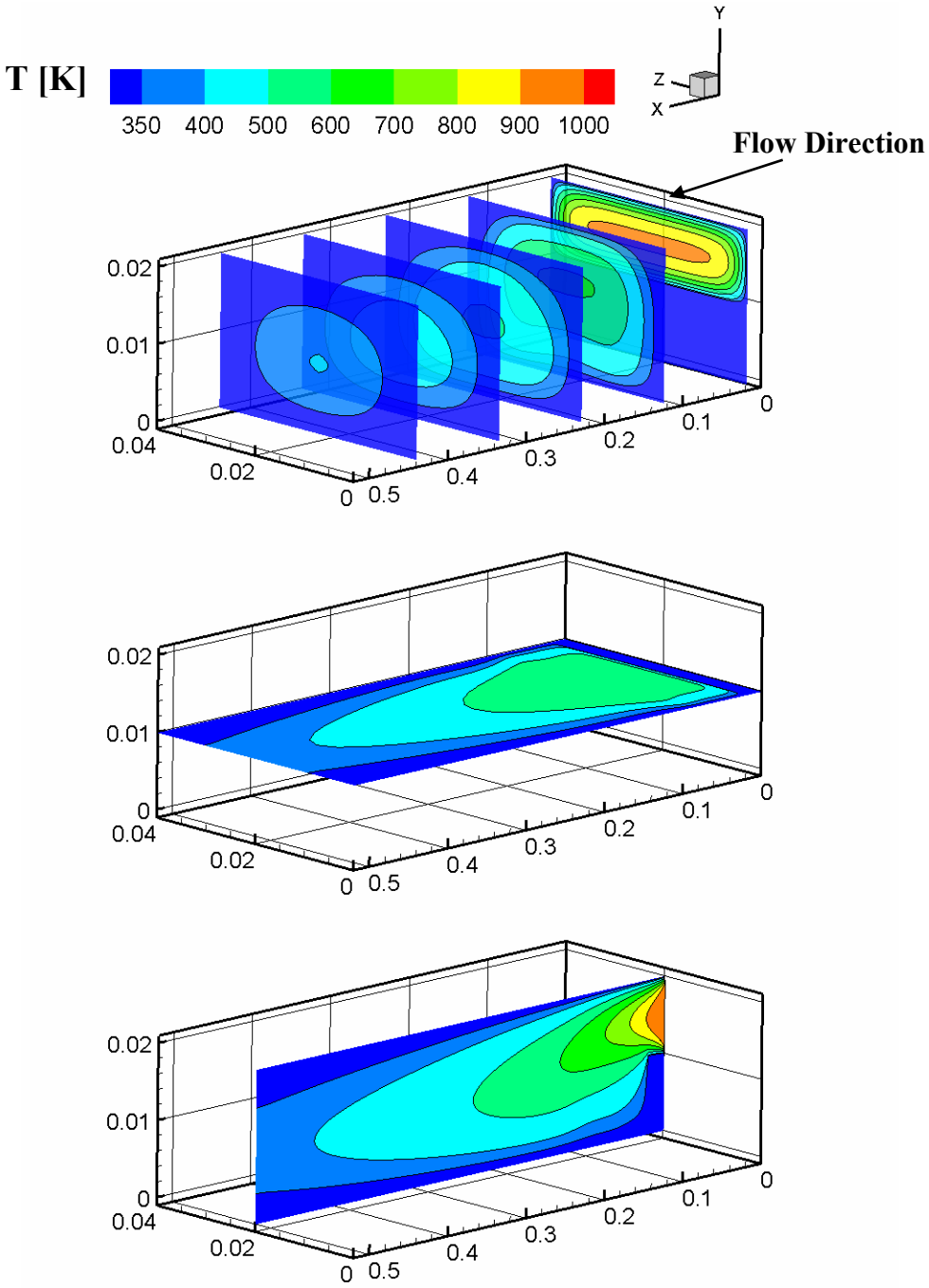

Figure 5.6. Temperature distributions for τ_H=0.4

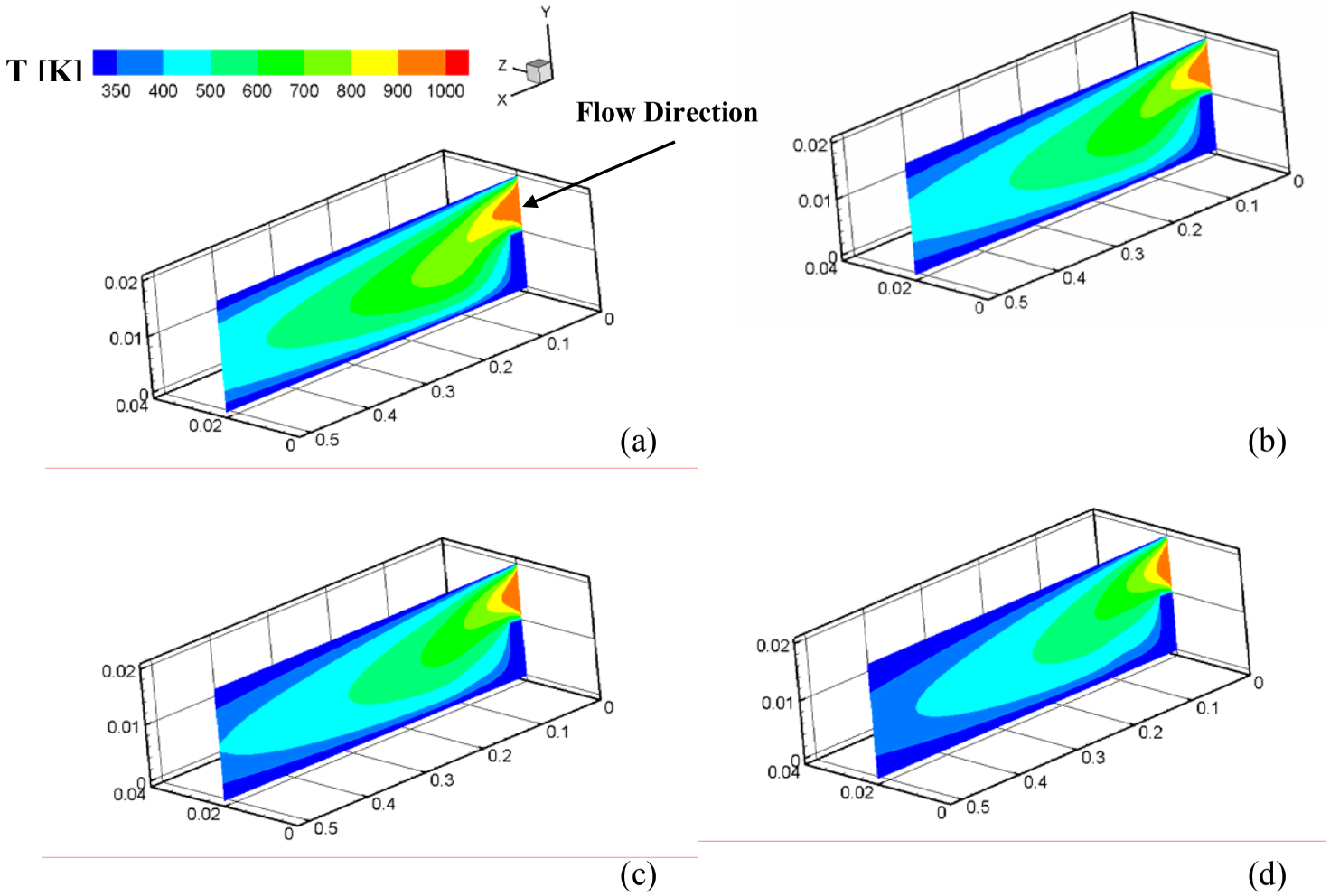

Figure 5.7. Effect of optical thickness on temperature distribution at constant z-plane (z=0.02): (a) without radiation; (b) τ_H=0.1; (c) τ_H=0.2; (d) τ_H=0.4

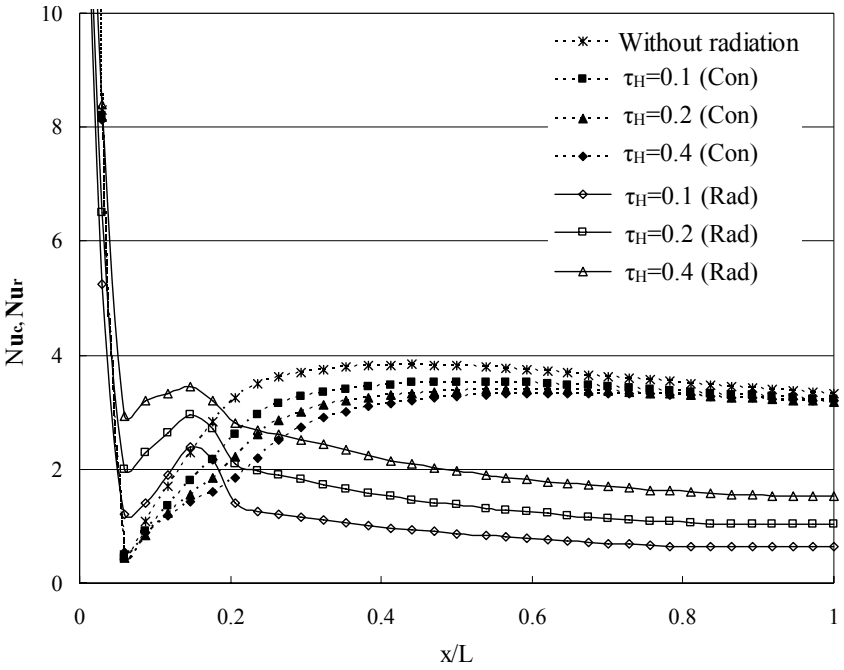

(a)

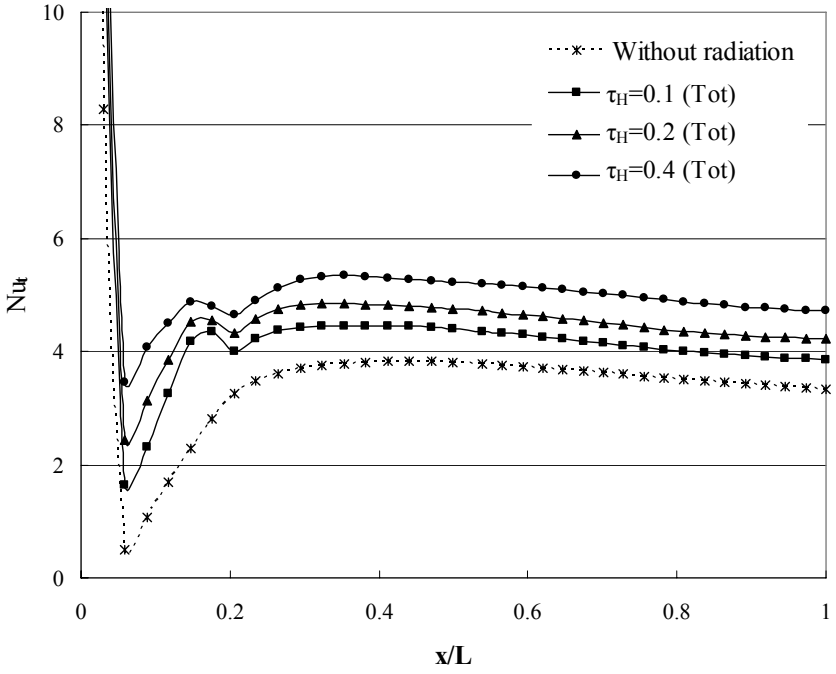

(b)

Figure 5.8. Span-wise averaged Nusselt number variation:
(a) convective and radiative Nu; (b) total Nu

With a decrease in kinematic viscosity by a factor of 7.6 and bulk velocity by a factor of 6.67 Reynolds number increase by a factor of 1.15. Thus, the bulk temperature decreases in the direction of flow resulting in an increase in the Reynolds number. As a result the recirculation zone expands and the *Xu*-line shifts further downstream with an increase in optical thickness (Figure 5.1(b)).

Figure 5.4 presents the U velocity component for the central plane in the span-wise direction (z/W=0.5) at different x positions for pure forced convection and combined convective radiative flow with τ_H=0.4. The flow was fully developed at the inlet. Downstream of the backward-facing step, U velocity components have negative values near the bottom wall because of the recirculation of flow. This effect is much more significant for the case of combined convection and radiation due to the expansion of the recirculation zone.

Results for the temperature distribution for the force convection and the case of τ_H =0.4 are presented along different planes in Figures 5.5 and 5.6, respectively. For both the forced convection and combined convection and radiation (τ_H=0.4) the temperature decreases along the channel. As expected, fluid is much cooler near the wall compared to the interior of the channel. Figure 5.7 shows the temperature contours for each value of the optical thickness. It is evident that the thermal penetration increases with increase in optical thickness.

Figure 5.8 presents the effect of optical thickness on Nusselt numbers. Note that the definitions of convective, radiative, and total Nusselt number are different. At the entrance the convective and radiative Nusselt number distributions have the highest

value and then dramatically decrease. Near the step a rapid change in both convective and radiative Nusselt number variations were found because of the sudden geometrical change. Figure 5.8(a) shows that Nu_c slightly decreases with an increase in optical thickness and Nu_r increases with an increase in optical thickness. It is evident from Figure 5.8(b) that Nu_t increases with an increase in optical thickness. This is to be expected as an increase in optical thickness implies that the radiation effect is dominant compared to the convective effect. Therefore Nu_c decreases slightly with an increase in optical thickness, but Nu_r increases much more resulting in an increase in Nu_t.

5.3 Effect of Scattering Albedo

The effect of scattering albedo (ω =0, 0.25, 0.5, 0.75, and 1) on the bulk temperature and reattachment length distribution for τ_H =0.2, *Re*=200, $T_w = 300K$, and $T_{in} = 1,000K$ are shown in Figure 5.9. The scattering albedo (ω) is defined as $\omega = \sigma/(\kappa + \sigma)$, ω =0 implies pure absorption (no scattering), and κ =0 implies pure scattering (ω =1). As ω increases from 0 to 1 the medium changes from pure absorption to pure scattering. Thus the bulk temperature gradually decreases from inlet to outlet with an increase in ω (Figure 5.9(a)). This is attributed to the fact that less radiative energy is converted to thermal energy in a pure scattering case compared to a pure absorption case. For reasons discussed in reference to Figure 5.1 a decrease in bulk temperature results in an increase in the size of the recirculation zone shifting the *Xu*-line further downstream. Hence, a decrease in ω leads to a shift in the *Xu*-line further downstream.

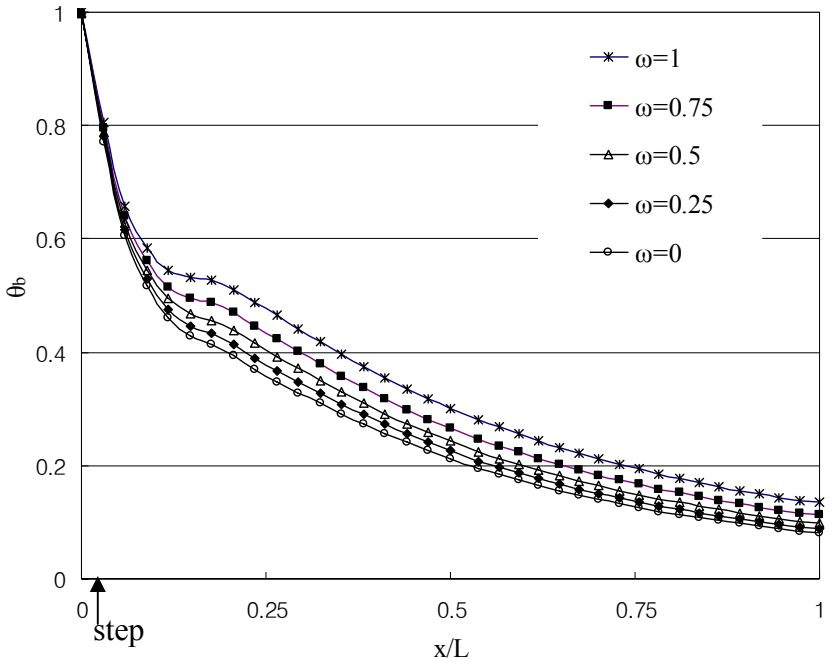

(a)

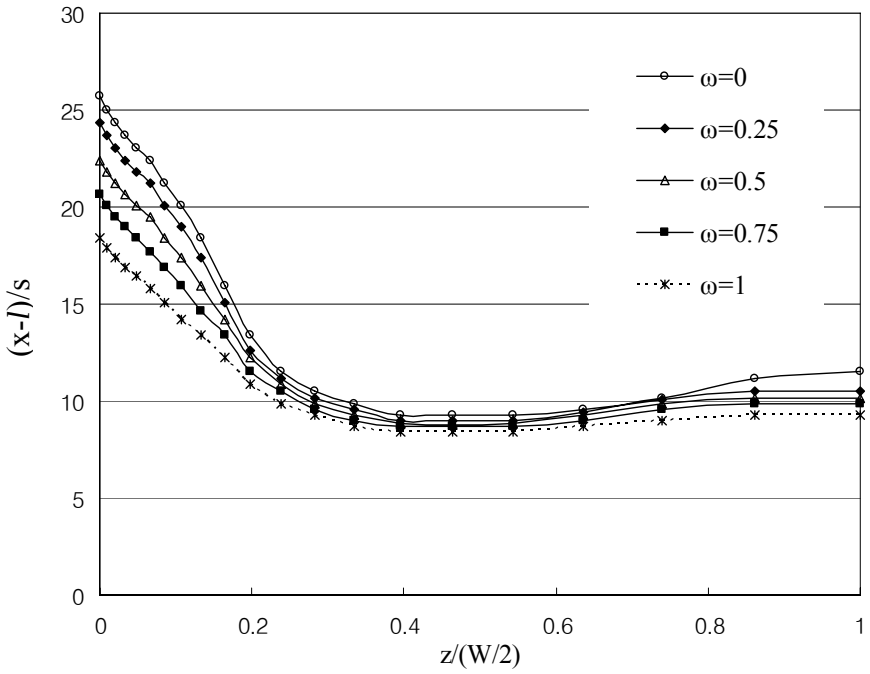

(b)

Figure 5.9. Effect of scattering albedo (ω=0, 0.25, 0.5, 0.75 and 1): (a) bulk mean temperature; (b) *Xu*-line distribution

Figures 5.10 and 5.11 show density and viscosity variations with scattering albedo along the central plane (z/W=0.5). The density of the fluid is high at the walls and low towards the exit of the channel. The density increases from 0.35 to 1.16 kg/m^3 resulting in the variation of density by a factor of 3.3 in the temperature range of 1,000K to 300K. As discussed earlier ω=0 corresponds to pure absorption and ω=1 corresponds to the pure scattering. Accordingly, the extent of cooling (thermal penetration) is much smaller for ω=1 compared to ω=0. Hence, density variations are much steeper for the case of ω=0. For the same reasons, a decrease in the dynamic viscosity value is much steeper for the case of ω=0 (Figure 5.11).

Figure 5.12 presents the U velocity component for the central plane in the span-wise direction (z/W=0.5) at different x positions for pure scattering (ω=1) and pure absorption cases (ω=0). As discussed earlier, a decrease in bulk temperature results in an increase in the size of the recirculation zone shifting the *Xu*-line further downstream. Therefore, it is evident that ω=0 results in fully developed state further downstream than that for ω=1.

Figure 5.13 shows the temperature contours for each value of scattering albedo. Nusselt number variation along the channel is shown in Figure 5.14. The Nu_c distributions for each case are not much different from each other. The Nu_r increased with a decrease in scattering albedo due to radiation dominance in the media. The Nu_t for ω=0 is the largest among these cases, although Nuc is the smallest.

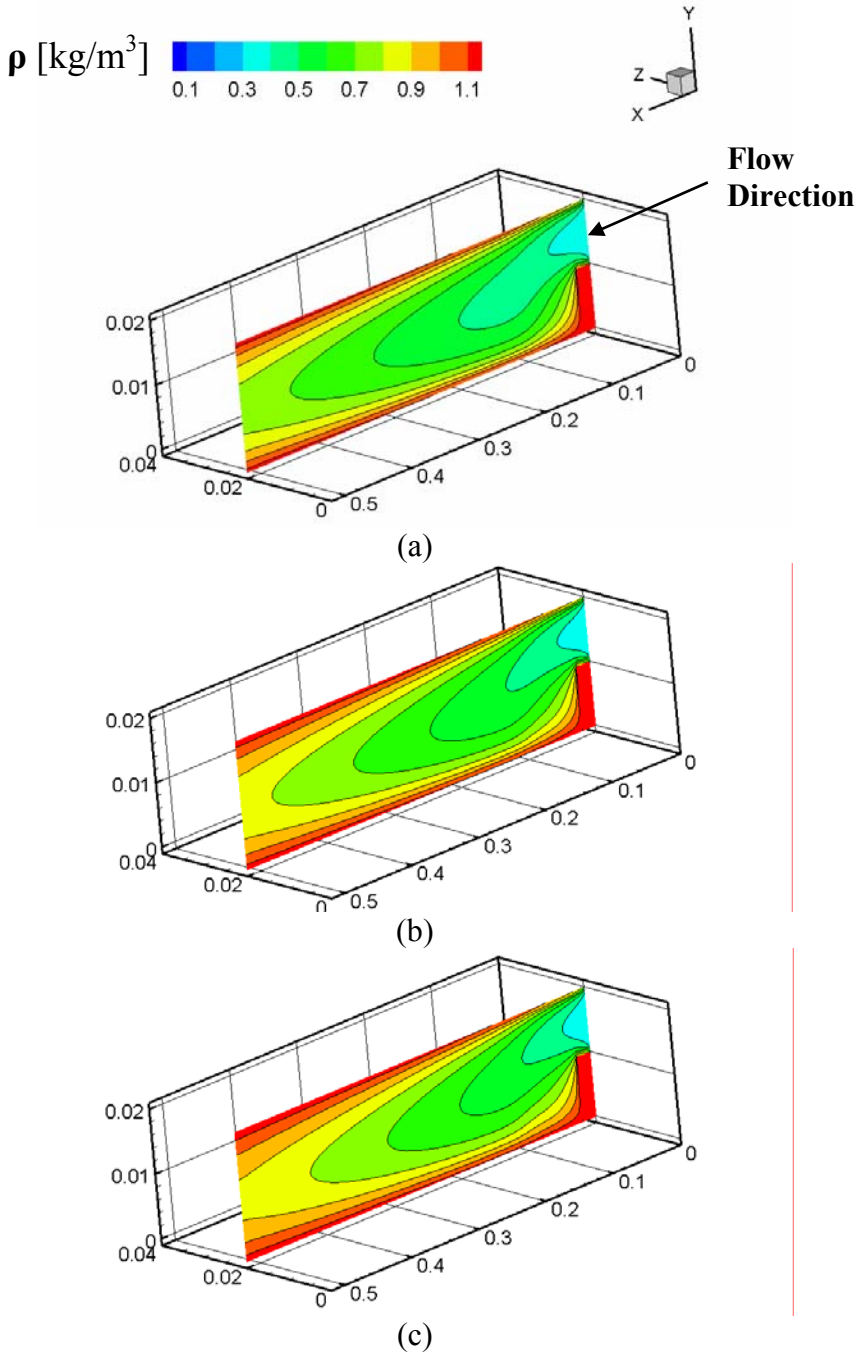

Figure 5.10. Density distributions at constant z-plane (z=0.02): (a) ω=1; (b) ω=0.5; (c) ω=0

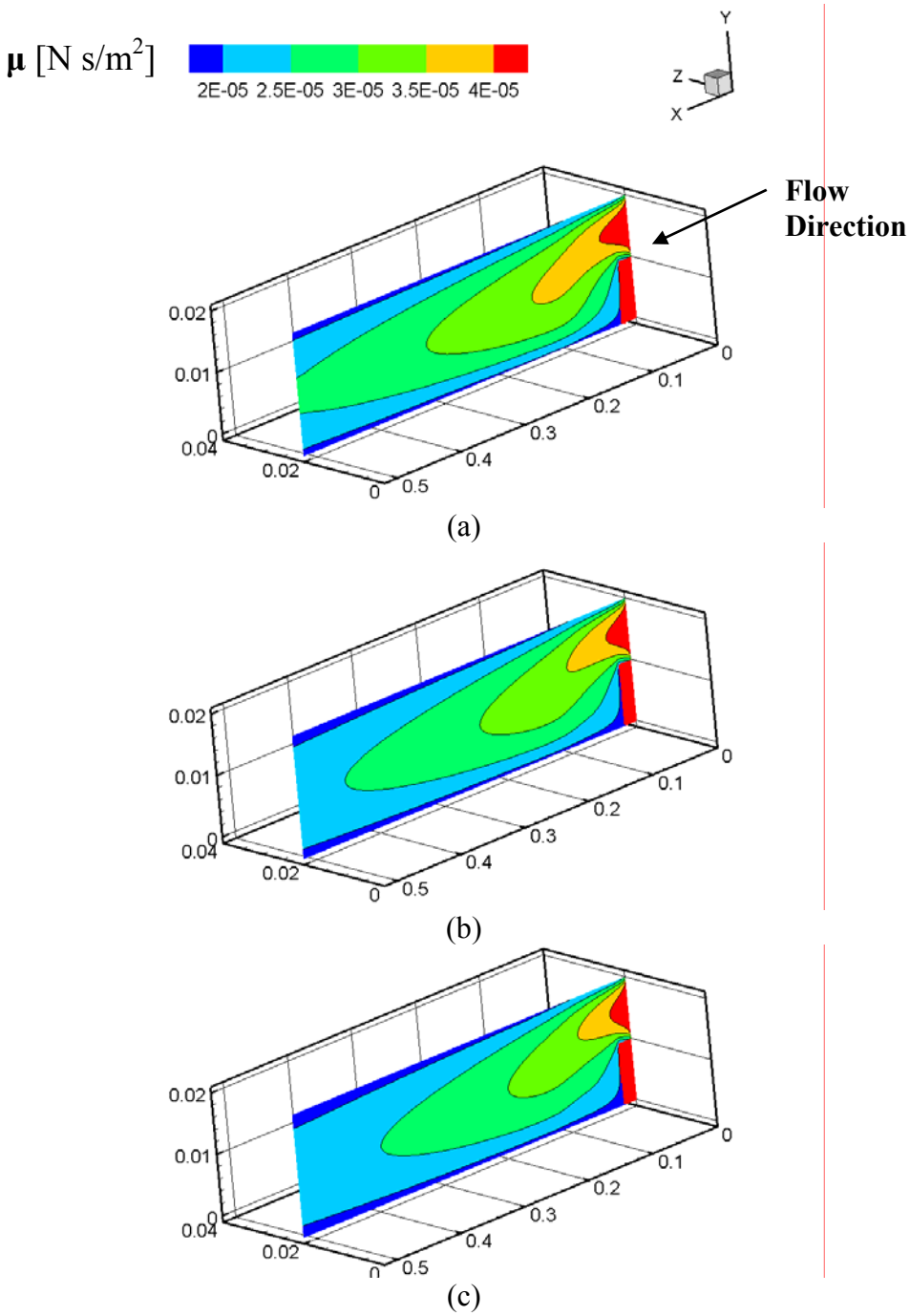

Figure 5.11. Viscosity distributions at constant z-plane (z=0.02): (a) ω=1; (b) ω=0.5; (c) ω=0

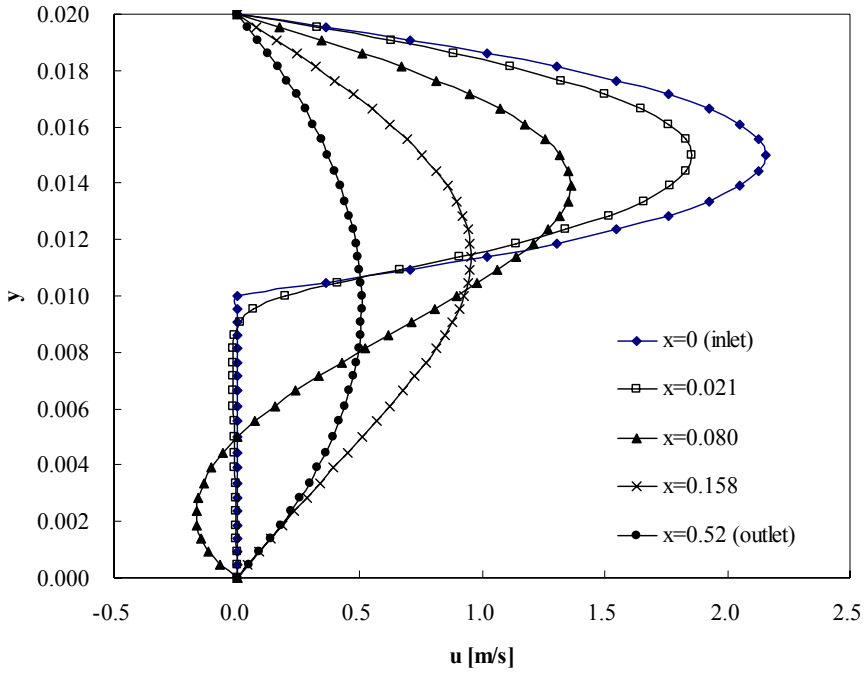

(a)

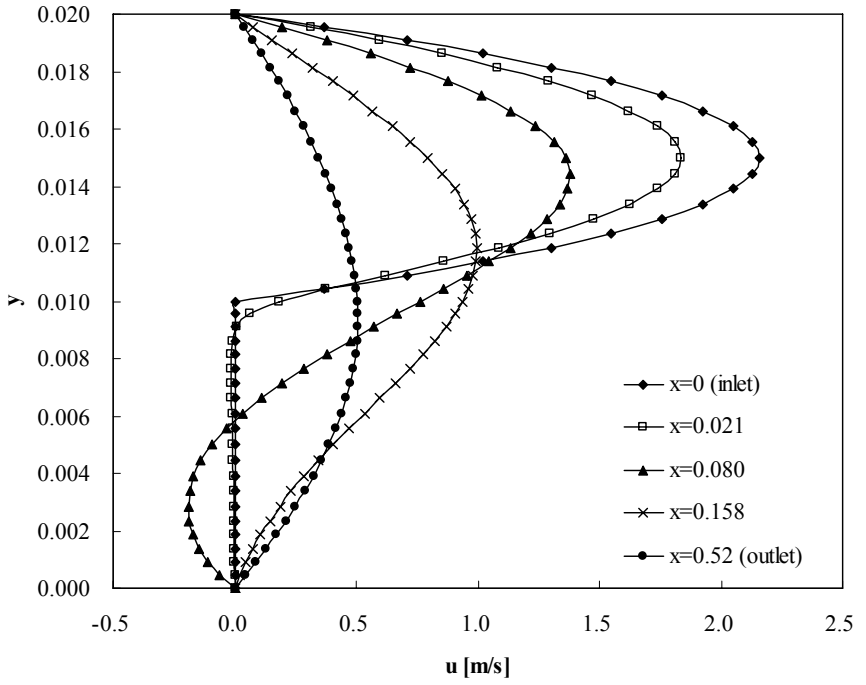

(b)

Figure 5.12. U-velocity profile at plane z=0.02 at different x positions: (a) ω=1; (b) ω=0

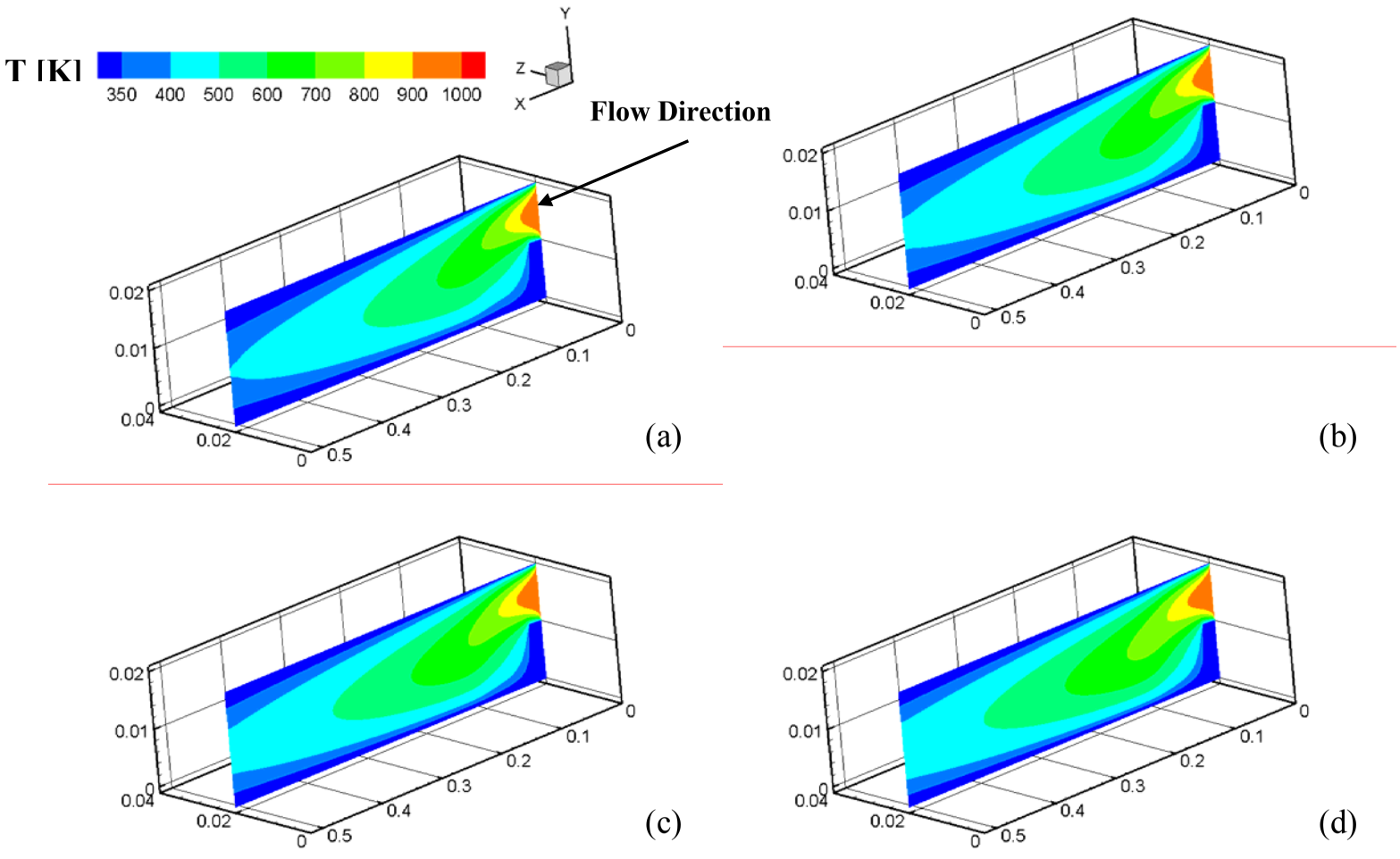

Figure 5.13. Effect of scattering albedo on temperature distribution at constant z-plane (z=0.02):
(a) ω=0; (b) ω=0.25; (c) ω=0.5; (d) ω=0.75

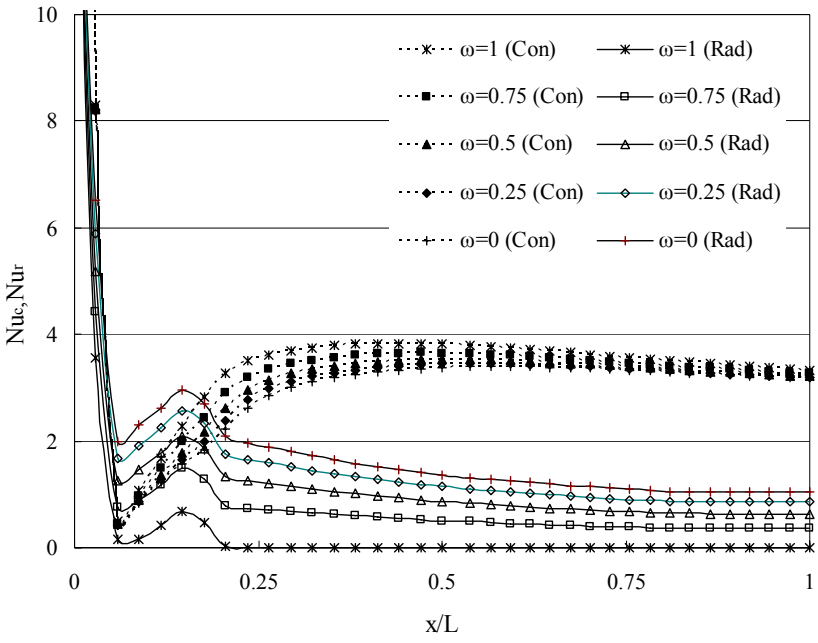

(a)

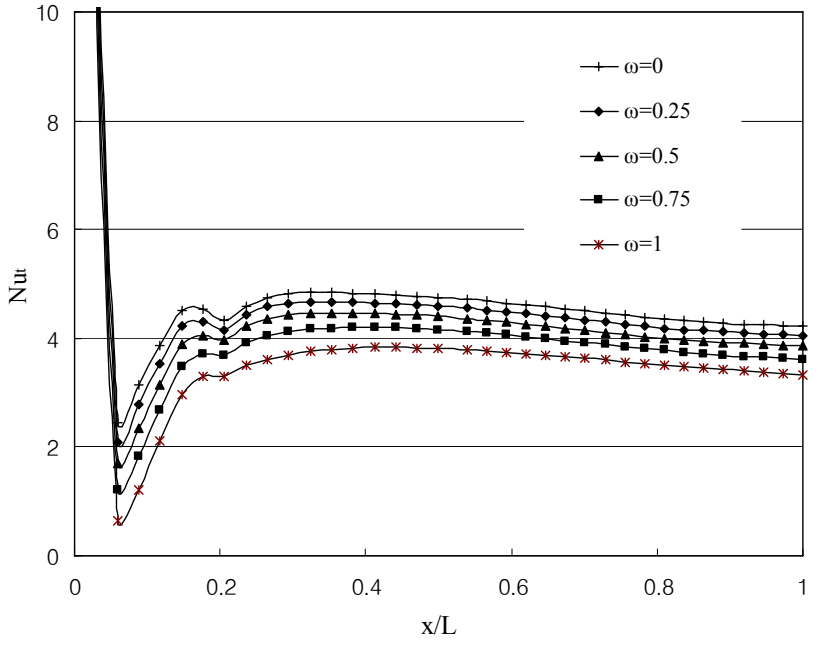

(b)

Figure 5.14. Span-wise averaged Nusselt number variation: (a) convective and radiative Nu; (b) total Nu

6. CONCLUSIONS

The present study investigates the characteristics of a combined forced convection and radiation problem in a three-dimensional channel with a horizontal backward-facing step. A finite volume based FORTRAN code was developed to simulate the flow and radiative heat transfer in the Cartesian coordinates. A detailed analysis for the distribution of reattachment length, bulk temperature, and Nusselt number was carried out to investigate the radiation effect on fluid flow and heat transfer.

Temperature distribution was influenced by radiation, depending on the absorption coefficient and the temperature, and was very different from that of pure forced convection. The radiation effects decrease with an increase in scattering albedo and a decrease in optical thickness. This reduction in radiation effects decreases thermal penetration. The fluid bulk temperature decreases with an increase in optical thickness or a decrease in scattering albedo which results in a decrease in kinematic viscosity which in turn increases the flow Reynolds number. An increase in Reynolds number implies dominance of inertial effects over viscous effects leading to an increase in the size of the recirculation zone shifting the *Xu*-line further downstream. An increase in optical thickness and decrease in scattering albedo represents the radiation dominance in the media. Therefore, the effect of radiative Nusselt number is greater than that of convective Nusselt number on total Nusselt number in the present study.

REFERENCES

1. A. T. Wassel, Molecular Gas Radiation and Laminar or Turbulent Heat Diffusion in a Cylinder with Internal Heat Generation, *Int. J. Heat Transfer*, vol. 18, pp. 1267-1276, 1975.
2. K. M. Im and R. K. Ahluwalia, Radiative Transfer in Spectrally Dissimilar Absorbing-Emitting-Scattering Adjacent Mediums, *AIAA J.*, vol. 21, no.1, pp. 134-141, 1983.
3. K. M. Im and R. K. Ahluwalia, Combined Convection and Radiation in Rectangular Ducts, *Int. J. Heat Mass Transfer*, vol. 27, pp. 221-231, 1984.
4. M. Kassemi and B. T. F. Chung, Two-Dimensional Convection and Radiation with Scattering from a Poiseuille Flow, *J. Thermophys.*, vol. 4, pp. 98-105, 1990.
5. T. K. Kim and H. S. Lee, Two-Dimensional Anisotropic Scattering Radiation in a Thermally Developing Poiseuille Flow, *J. Thermophys. Heat Transfer*, vol. 4, pp. 292-298, 1990.
6. T. Seo, D. A. Kaminski, and M. K. Jensen, Combined Convection and Radiation in Simultaneously Developing Flow and Heat Transfer with Nongray Gas Mixture, *Numer. Heat Transfer A*, vol. 26, pp. 49-66, 1994.
7. M. Y. Kim and S. W. Baek, Numerical Analysis of Conduction, Convection, and Radiation in a Gradually Expanding Channel, *Numer. Heat Transfer A*, vol. 29, pp. 725-740, 1996.

8. E. Sediki, A. Soufiani, and M. S. Sifaoui, Combined Gas Radiation and Laminar Mixed Convection in Vertical Circular Tubes, *Int. J. Heat Mass Fluid Flow*, vol. 24, pp. 736-746, 2003.
9. H. C. Chiu, J. H. Jang, and W. M. Yan, Mixed Convection Heat Transfer in Horizontal Rectangular Ducts with Radiation Effects, *Int. J. Heat Mass Transfer*, vol. 50, pp. 2874-2882, 2007.
10. J. C. Chai, H. S. Lee, and S. V. Patankar, Laminar Heat Transfer of a Radiating Fluid in a Backward Facing Step Flow, *Proceedings of Transport Phenomena in Thermal Engineering*, pp. 209-214, 1993.
11. H. C. Hottel and E. S. Cohen, Radiant Heat Exchange in a Gas-filled Enclosure: Allowance for Nonuniformity of Gas Temperature, *AICHE Journal*, vol. 4. pp. 3-14, 1958.
12. M. H. N. Naraghi and M. Kassemi, Radiation Transfer in Rectangular Enclosures: A Discrete Exchange Factor Solution, *J. Heat Transfer*, vol. 111, pp. 1117-1119, 1989.
13. J. R. Howell and M. Perlmutter, Monte Carlo Solution of Thermal Transfer through Fadiant Media between Gray Walls, *J. Heat Transfer*, vol. 86, pp. 116-122, 1964.
14. J. H. Jeans, The Equation of Radiative Transfer of Energy, *Monthly Notices Royal Astronomical Society*, vol. 78, pp. 28-36, 1917.
15. M. P. Menguc and R. Viskanta, Radiative Transfer in Three-Dimensional Rectangular Enclosures Containing Inhomogeneous, Anisotropic Scattering Media, *J. Quant. Spectrosc. Radiat. Transfer*, vol. 33, pp. 533-549, 1985.

16. M. P. Menguc and R. Viskanta, Radiative Transfer in Axisymmetric, Finite Cylindrical Enclosures, *J. Heat Transfer*, vol. 108, pp. 271-276, 1986.
17. S. Chandrasekhar, *Radiative Transfer*, Dover Publication, Inc., New York, 1960.
18. J. C. Chai, H. S. Lee, and S. V. Patankar, Ray Effect and False Scattering in the Discrete Ordinates Method, *Numer. Heat Transfer B*, vol. 24, pp. 373-389, 1993.
19. E. H. Chui and G. D. Raithby, Computation of Radiant Heat Transfer on a Nonorthogonal Mesh Using the Finite Volume Method, *Numer. Heat Transfer B*, vol. 23, pp. 269-288, 1993.
20. J. C. Chai, H. S. Lee, and S. V. Patankar, Finite-Volume Method for Radiation Heat Transfer, *J. Thermophy.*, vol. 8, pp. 419-425, 1994.
21. H. S. Li, G. Flamant, and J. D. Lu, Reduction of False Scattering of the Discrete Ordinate Method, *J. Heat Transfer*, vol. 124, pp. 837-844, 2002.
22. B. F. Armaly and A. Li, and J. H. Nie, Measurements in Three-Dimensional Laminar Separated Flow, *Int. J. Heat Mass Transfer*, vol. 46, pp. 3573-3582, 2003.
23. B. F. Blackwell and D. W. Pepper, Benchmark Problems for Heat Transfer Codes, *ASME HTD*, vol. 222, ASME, New York, 1992.
24. B. F. Blackwell and B. F. Armaly, Computational Aspects of Heat Transfer-Benchmark Problems, *ASME HTD*, vol. 258, ASME, New York, 1993.
25. M. Ko and N. K. Anand, Numerical Simulation of Three-Dimensional Combined Convective Radiative Heat Transfer - a Finite Volume Methood, *International Journal for Computational Methods in Engineering. Science and Mechanics*, vol. 8, pp. 429-437, 2007.

26. J. G. Barbosa-Saldana, N. K. Anand, and V. Sarin, Numerical Simulation of Mixed Convective Flow over a Three-Dimensional Horizontal Backward-Facing Step, *J. Heat Transfer*, vol. 127, pp. 1027-1036, 2005.

27. F. P. Incropera and D. P. Dewitt, *Fundamentals of Heat and Mass Transfer, 4th Edition*, John Wiley & Sons, New York, 1996.

28. W. J. Minkowycz, E. M. Sparrow, and J. Y. Murthy, *Handbook of Numerical Heat Transfer,* 2nd Edition, John Wiley & Sons, New York, 2006.

29. M. N. Ozisik, *Radiative Transfer: A Wiley-Interscience Publication*, Wiley, New York, 1973.

30. J. C. Chai, *A Finite-Volume Method for Radiation Heat Transfer*, Ph. D. Dissertation, University of Minnesota, Minneapolis, MN, 1994.

31. S. V. Patankar. *Computation of Conduction and Duct Flow Heat Transfer*, Innovative Research, INC, Minneapolis, 1991.

32. X. Chen and P. Han, A Note on the Solution of Conjugate Heat Transfer Problems Using SIMPLE-Like Algorithm, *Int. J. Heat Fluid Flow*, vol. 21, pp. 463-467, 2000.

33. J. C. Chai, H. S. Lee, and S. V. Patankar, Treatment of Irregular Geometries Using a Cartesian Coordinates Finite-Volume Radiation Heat Transfer Procedure, *Numer. Heat Transfer B*, vol. 26, pp. 225-235, 1994.

34. R. K. Shah and A. L. London, *Laminar Flow Forced Convection in Ducts*, Academic Press, New York, 1978.

35. S. V. Patankar, *Numerical Heat Transfer and Fluid Flow*, Taylor and Francis, Philadelphia, 1981.

36. F. H. Harlow and E. Welch, Numerical Calculation of Time-Dependent Viscous Incompressible Flow of Fluid with Free Surface, *Physics of Fluid*, vol. 8, pp. 2182-2189, 1965.

37. H. K. Versteeg and W. Malalasekera, *An introduction to Computational Fluid Dynamics: The Finite Volume Method*, Prentice Hall, London, 1995.

38. J. H. Ferziger and M. Peric, *Computational Methods for Fluid Dynamics*, Springer-Verlag, Berlin, 1997.

39. E. H. Chui, G. D. Raithby, and P. M. J. Hughes, Prediction of Radiative Transfer in Cylindrical Enclosures with the Finite Volume Method, *J. Thermophy. Heat Transfer*, vol. 6, pp. 605-611, 1992.

40. P. Talukdar, M. Steven, F. V. Issendorff, and D. Trimis, Finite Volume Method in 3-D Curvilinear Coordinates with Multiblocking Procedure for Radiative Transport Problems, *Int. J. Heat Mass Transfer*, vol. 48, pp. 4657-4666, 2005.

41. S. C. Chapra and R. P. Canale, *Numerical Method for Engineers*, 4th ed., McGraw Hill, Boston, 2002.

42. N. Kim, N. K. Anand, and D. L. Rhode, A Study on Convergence Criteria for a SIMPLE-Based Finite Volume Algorithm, *Numer. Heat TransferB,* vol. 34, pp. 401-417, 1998.

43. J. H. Nie and B. F. Armaly, Reattachment of Three-Dimensional Flow Adjacent to Backward-Facing Step, *J. Heat Transfer*, vol. 125, pp. 422-428, 2003.

APPENDIX A

NUMERICAL SIMULATION OF THREE-DIMENSIONAL COMBINED CONVECTIVE RADIATIVE HEAT TRANSFER - A FINITE VOLUME METHOD*

A.1 Abstract

Combined laminar forced convection and radiation heat transfer was numerically simulated in a three-dimensional channel flow. A finite volume method was used to solve the steady incompressible Navier-Stokes equations, energy equation, and radiative transfer equation. The effects of Reynolds number, conduction-radiation parameters, absorption coefficient, and scattering albedo on the Nusselt number and bulk temperature profiles along the channel are presented. Radiation was found to play a major impact on temperature field in the range of parameters considered in this study. It was found that the radiation effect is diminished, and thermal penetration is increased with increasing Reynolds number, conduction-radiation parameter, scattering albedo, and decreasing absorption coefficient.

* Reprinted with permission from "Numerical Simulation of Three-Dimensional Combined Convective Radiative Heat Transfer-A Finite Volume Method" by M. Ko and N. K. Anand, International Journal of Computational Methods in Engineering Science and Mechanics, 8: 429-437, 2007, © Taylor & Francis Group, LLC.

A.2 Nomenclature

C_j	expansion coefficient	ε	emissivity
C_p	specific heat of fluid	κ	absorption coefficient
D_{cx}, D_{cy}, D_{cz}	defined quantities, Eqs. (A.14)-(A.16)	μ	dynamic viscosity
D_h	hydraulic diameter	Φ	scattering phase function
f	friction factor	$\Phi^{l'l}$	average energy scattered from control angle l' to l
G	incident radiation	ϕ	azimuthal angle
I	radiative intensity	ρ	density
I_b	blackbody intensity	σ	scattering coefficient
k	thermal conductivity of fluid	σ_s	Stefan-Boltzmann constant
L_x, L_y, L_z	total length of channel in x,y,z directions	τ_{DH}	optical thickness
N_{cr}	conduction-radiation parameter	θ	polar angle
Nu	Nusselt number	ω	scattering albedo
Nu_x	local Nusselt number	Ψ	scattering angle
P	pressure	ξ	general variable
Pe	Peclet number		
R_u, R_v, R_w	residual for U,V,W	**Subscripts**	
R_p	residual for pressure		
s	traveled distance	i, j, k	indices of nodes in x,y,z directions
S_c, S_p	defined quantities, Eqs (A.23 and A.24)	nb	neighbor point
S_m^l	modified source function	p	central grid point
U,V,W	velocity component in x,y,z direction	w,e,s,n,b,t	west, east, south, north, bottom, and top
U_{in}	inlet velocity		
T	temperature		
T_b	bulk temperature	**Superscript**	
T_{in}	inlet temperature		
T_w	wall temperature	l', l	l' and l direction in control angle
β_m^l	modified extinction coefficient		
$\Delta\Omega$	solid angle		

A.3 Introduction

In various thermal engineering systems, such as glass manufacturing, oil or gas-fired boilers, and in high temperature technological applications, interaction of conductive, convective and radiative heat transfer are important. In such situations, the conduction, convection and radiation modes in heat transfer must be considered in order to determine the velocity and temperature profiles.

Heat transfer problems involving combined modes have been extensively studied and published in the literature. Wassel studied combined non-gray radiation and thermal diffusion for laminar and turbulent flows with uniform internal heat generation. He solved the integro-differential thermal equation using the Galerkin method for the laminar flow case and finite difference method for turbulent flow case. Im and Ahluwalia analyzed combined convective and radiative heat transfer in a rectangular duct by solving simultaneously the flow and radiative transport equations. They used the method of moments to simplify a radiative heat transfer equation. Kassemi and Chung reported the combined effects of laminar forced convection and various radiation effects on the flow in a two-dimensional rectangular channel. Fluid was considered to be absorbing, emitting, and isotropically scattering. They also presented a numerical model by a set of coupled nonlinear integro-partial differential equations using an element-to-node approach. Kim and Lee studied a thermally developing Poiseuille flow with anisotropic scattering medium between two infinite parallel plates. They considered gray absorbing, emitting, and anisotropic fluid flow. Chai et al. discussed the effect of radiation in a two dimensional channel flow with a backward facing step and used the

discrete ordinates method to solve radiative heat transfer equation. They presented various effects important to combined mode heat transfer, but their work only showed isotherms for all cases. Their work did not show detailed heat transfer analysis; e.g. variation of Nusselt number and bulk temperature along the flow direction and the effect of variation of wall emissivity and temperature.

Among the methods to solve the radiative heat transfer with participating media, the finite volume method has been used. If the finite volume method is used for radiation calculation, the procedure is very efficient because a radiation heat transfer calculation procedure can share the same computational grid as used for other dependent variables in the finite volume method, and we have full flexibility in positioning the spatial and angular grids. Mezrhab et al. described a numerical study of the radiation-natural convection interaction in a differentially heated cavity with an inner body. They developed a finite volume method for the solutions of the governing differential equations and discussed the radiation and convection interaction. Chiu et al. studied numerically the mixed convective heat transfer with radiation effects in a horizontal duct. They used a discrete ordinates method to solve a radiative transfer equation and the vorticity-velocity method to solve the momentum and energy equation simultaneously. The effects of buoyancy force and radiation on temperature, friction factor, and Nusselt number were presented.

The above cited references show that in the past investigators have tried to solve the combined mode heat transfer equations with participating media. However, most of them were confined to solve a two-dimensional model for a combined heat transfer problem.

The main objective of this study is to present and understand the effects of combined conduction, convection, and radiation on temperature field of a flow in a three-dimensional channel using a finite volume method. Contributions in the present paper differs from the ones in the literature in the following ways: (1) this is the first attempt to study combined convection-radiation in a 3-D channel using a finite volume technique, (2) span-wise averaged local Nusselt number and bulk temperature are presented for combined convection and radiation in presence of a participating medium, and (3) the present paper serves as validation for us to study 3-D combined convection-radiation in Cartesian geometry. In this respect the present contribution has both research and tutorial value. We have developed a numerical code that can handle absorbing-emitting, isotropic or anisotropic scattering, gray, and heat generating medium and showed the effect of various dimensionless parameters and wall temperature on Nusselt number and bulk temperature along the channel or cross section.

In the following sections, the governing equation for flow fields and radiative heat transfer equations, development of a finite volume technique and solution methodology, validation and grid independence of the algorithm, and result of various independent parameters on temperature field are presented.

A.4 Problem Formulation

Figure A.1 shows the geometry under consideration. The axial length of the channel is equal to 20 times the hydraulic diameter of the channel. In this study, three-dimensional laminar incompressible flow and temperature fields are simulated. Variation

of thermophysical properties of the fluid was accounted for using piecewise-linear function of temperature. The medium was assumed to be gray and viscous dissipation was neglected.

Based on these assumptions, the mass conservation, momentum, and energy equations governing the fluid motion and the temperature distribution expressed in the Cartesian coordinate can be written as:

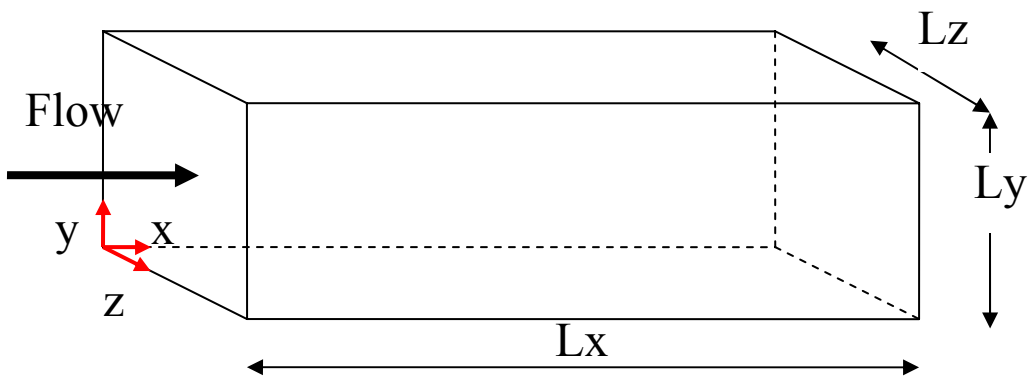

Figure A.1. Geometry

Continuity

$$\nabla \cdot \rho \vec{V} = 0 \tag{A.1}$$

Momentum

$$\rho \vec{V} \cdot \left(\nabla \vec{V} \right) = -\nabla P + \nabla \cdot \left(\mu \nabla \vec{V} \right) \tag{A.2}$$

Energy

$$\rho C_P \vec{V} \cdot \left(\nabla T \right) = \nabla \cdot \left(k \nabla T \right) - \kappa \left(4\sigma_s T^4 - \int_{4\pi} I d\Omega \right) \tag{A.3}$$

Note in the energy equation of Eq. (A.3) source term appears on the right-hand

side, $\kappa\left(4\sigma_s T^4 - \int_{4\pi} I d\Omega\right)$, which is the divergence of radiative heat flux, i.e.,

$$\nabla \cdot q = \kappa\left(4\sigma_s T^4 - \int_{4\pi} I d\Omega\right) = \kappa(4\pi I_b - G) \tag{A.4}$$

This radiative source term in energy equation is an important quantity in combined heat transfer cases with a participating media because this term is function of temperature and significantly affects the temperature distribution.

The linearized radiation transfer equation for absorbing, emitting, and scattering gray medium is defined as

$$\frac{dI^l}{ds} = -\beta_m^l I^l + S_m^l \tag{A.5}$$

where the superscript l represents the angular direction of interest. The radiant intensity I depends on spatial position and angular position. The modified extinction coefficient β_m^l and the modified source function S_m^l are defined as follows:

$$\beta_m^l = (\kappa + \sigma) - \frac{\sigma}{4\pi}\Phi^{ll}\Delta\Omega^l \tag{A.6}$$

$$S_m^l = \kappa I_b - \frac{\sigma}{4\pi}\sum_{l'=1, l'\neq l}^{L} \Phi^{l'l} I^{l'} \Delta\Omega^{l'} \tag{A.7}$$

where l' represents the in-scattering from all possible directions.

Approximately, the scattering phase function is defined by a finite series of Legendre polynomials as

$$\Phi^{l'l} = \Phi(\cos\Psi) = \sum_{j=0}^{K} C_j P_j(\cos\Psi) \tag{A.8}$$

Where Ψ is the scattering angle and represents the angle between radiation direction

l and l'. The C_j s are called the phase function expansion coefficients and Table A.1 gives these values for an isotropic and two anisotropic scattering phase functions used in this study. In Table A.1, F represents forward scattering phase functions, and B represents backward scattering phase functions. Further explanation about these phase function expansion coefficients can be found in Kim and Lee.

Fluid enters the domain with a uniform velocity and temperature, U_{in} and T_{in}, respectively, and the walls are maintained at temperature T_w. The difference between inlet (T_{in}) and wall (T_w) temperature is chosen such that the radiation effects in the channel will be significant. Because the values of thermophysical properties depend on temperature, the flow field is coupled with the energy field including radiation source term. To handle the temperature distribution in the radiative transfer equation, we set the inlet and outlet walls to be pseudo-black walls with prescribed temperature, T_{in} and T_w, respectively.

Air at a very high temperature relative to wall temperature enters the channel. The uniform inlet velocity, U_{in}, is computed by the Reynolds number and hydraulic diameter. With these settings, we studied the effect of independent parameters such as Reynolds number (Re), Planck number $\left(N_{cr} = \frac{k(\kappa+\sigma)}{4\sigma_s T_{in}^3} \right)$, absorption coefficient (κ), and scattering albedo ($\omega = \frac{\sigma}{\kappa+\sigma}$) on bulk temperature and Nusselt number along the channel.

Table A.1. The phase function expansion coefficients

j	Isotropic	F	B
0	1.000	1.000	1.000
1		2.536	-0.565
2		3.565	0.298
3		3.980	0.086
4		4.002	0.010
5		3.664	0.001
6		3.016	
7		2.233	
8		1.303	
9		0.535	
10		0.201	
11		0.055	
12		0.011	
Phase function asymmetry factor	0.000	0.845	-0.188

A.5 Solution Technique

Flow fields along with the related boundary conditions are solved using a finite volume method. In this procedure, the momentum and energy equation inside the computational domain are discretized. Pressure and velocity fields are linked by the SIMPLE algorithm. Solution to the one-dimensional convection diffusion equation is represented by the power law. All scalar properties including pressure and temperature are located at the main grid nodes. But the nodes for velocities are placed at staggered locations in each coordinate direction. At the exit, it is important to note that axial gradients of all variables are neglected and the ratio of overall mass flow in and out inside the domain are used for correcting the outlet velocities. The discretized equations for velocity component and pressure at each plane in Cartesian coordinates were solved

by the line-by-line method, which is a combination of the Tri-Diagonal Matrix Algorithm (TDMA) and the Gauss-Seidal procedure.

For computational stability under-relaxation factor was used for velocity variable in momentum equations. The momentum and pressure relaxation factors are set between 0.5 and 0.7. The convergence criteria for velocity components and pressure are defined as follows:

$$R_U = \frac{\sum_{nodes} \left| a_e U_e - \sum a_{nb} U_{nb} - A_e (P_P - P_E) \right|}{a_e U_e} \leq \varepsilon_u \tag{A.9}$$

$$R_V = \frac{\sum_{nodes} \left| a_n V_n - \sum a_{nb} V_{nb} - A_n (P_P - P_N) \right|}{a_n V_n} \leq \varepsilon_v \tag{A.10}$$

$$R_W = \frac{\sum_{nodes} \left| a_t W_t - \sum a_{nb} W_{nb} - A_t (P_P - P_T) \right|}{a_t W_t} \leq \varepsilon_w \tag{A.11}$$

$$R_P = \frac{\rho \sum_{nodes} \left| (U_w - U_e) dydz + (V_s - V_n) dxdz + (W_b - W_t) dxdy \right|}{\rho U_{in} L_x L_y} \leq \varepsilon_p \tag{A.12}$$

The convergence tolerance in this study is set to less than or equal to 1×10^{-6} for all variables.

A finite volume method proposed by Chai et al. is used to discretize the Eq. (A.5). The upwind scheme was used for a spatial differencing which is needed to relate the boundary intensities to the nodal intensities. The final discretization equation for the upwind scheme can be expressed as

$$I_p^l = \frac{D_{cx}^l I_W^l \Delta y \Delta z + D_{cy}^l I_S^l \Delta x \Delta z + D_{cz}^l I_B^l \Delta x \Delta y + \left(S_m^l\right)_P \Delta\Omega^l \Delta x \Delta y \Delta z}{D_{cx}^l \Delta y \Delta z + D_{cy}^l \Delta x \Delta z + D_{cz}^l \Delta x \Delta y + \left(\beta_m^l\right)_P \Delta\Omega^l \Delta x \Delta y \Delta z} \tag{A.13}$$

where

$$D_{cx}^l = \int (s^l \cdot n_x) d\Omega^l = \int_\theta \int_\phi \sin^2\theta \cos\phi \, d\theta d\phi \tag{A.14}$$

$$D_{cy}^l = \int (s^l \cdot n_y) d\Omega^l = \int_\theta \int_\phi \sin^2\theta \sin\phi \, d\theta d\phi \tag{A.15}$$

$$D_{cz}^l = \int (s^l \cdot n_z) d\Omega^l = \int_\theta \int_\phi \sin\theta \cos\theta \, d\theta d\phi \tag{A.16}$$

$$\Delta\Omega = \int_\theta \int_\phi \sin\theta \, d\theta d\phi \tag{A.17}$$

Angular direction shown in Figure A.2 is expressed as

$$s = (\sin\theta\cos\phi)\vec{i} + (\sin\theta\sin\phi)\vec{j} + \cos\theta\vec{k} \tag{A.18}$$

A detailed procedure for the discretization of equation using a finite volume method is given in Chai and Patankar. Using Eq. (A.13) and related boundary conditions, the radiative intensity fields are obtained.

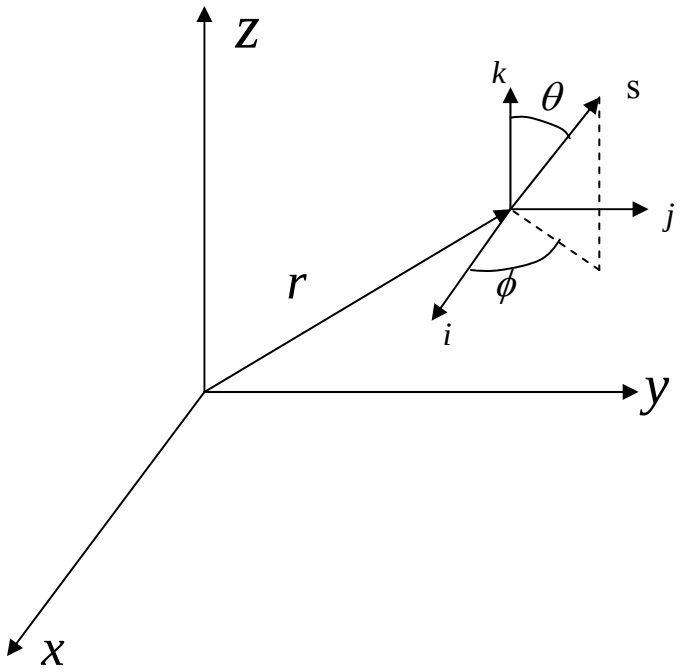

Figure A.2. Angular direction

.

The energy equation for forced convection, Eq. (A.3), is solved with the velocity fields and radiative source term. Because the radiative source term in the energy equation depends on temperature, we must express the dependence in a linear form to avoid the numerical instabilities. In a finite volume discretization technique the source term is transformed through a linearization as shown below

$$\overline{S}_{\phi} = S_c + S_p \phi_p \tag{A.19}$$

Considering this source term linearization method, the final discretized energy equation is expressed as

$$a_p T_p = \sum a_{nb} T_{nb} + b \tag{A.20}$$

where

$$a_P = a_W + a_E + a_S + a_N + a_B + a_T - S_p \Delta x \Delta y \Delta z \tag{A.21}$$

$$b = S_c \Delta x \Delta y \Delta z \tag{A.22}$$

$$S_c = \frac{(1-\omega)\beta}{\rho C_p}\left(12\sigma_s \tilde{T}_p^4 + G\right) \tag{A.23}$$

$$S_p = -\frac{16\sigma_s(1-\omega)\beta}{\rho C_p} \tag{A.24}$$

and the coefficients for the all nodal points, a_i, are given in Patankar.

The numerical computing order in this study is as follows. It starts with the solution of momentum equations. After the velocity and pressure fields are obtained, we start to solve the linearized radiative heat transfer equation to calculate radiative intensities. When the maximum relative change of the radiative intensities falls below the prescribed value, the intensities are stored for the initial values for the radiative heat transfer equation in the next iteration, and the incident radiation energy is calculated and used in the energy source term. After we calculate the temperature distribution from the energy equation, all thermophysical properties are updated. This procedure is repeated until the temperature between two successive iterations is less than or equal to a prescribed value. The definition for convergence criteria used for radiative intensity and temperature is presented as follows:

$$R_\phi = \left| \frac{\xi_{i,j,k}^{n+1} - \xi_{i,j,k}^{n}}{\xi_{i,j,k}^{n+1}} \right| \le 10^{-6} \tag{A.25}$$

This is also equivalent to monitoring the residuals as shown by Kim et al.

A.6 Validation and Grid Independence

A reference case of the fully developed fluid flow problem for a rectangular duct is used to validate the current 3-D code. Shah and London compiled data of flow and heat transfer for various cases. The friction factor and Nusselt number for rectangular duct are used for validation of our code. In present 3-D code the source term in the energy equation, Eq. (A.4), was set to zero so that the temperature field could be compared with the ones by Shah and London for fully developed flow in a straight channel of arbitrary length. The product of friction factor *f* and Re for fully developed laminar flow through a square channel is 57.048. The peripheral average local Nusselt number for constant wall temperature case is calculated using the following definition for a straight channel:

$$Nu_x = \frac{D_h \left(\left(\frac{\partial T}{\partial n} \right)_w \right)_x}{T_w - T_b} \tag{A.26}$$

The parameters given by Shah and London are compared with those calculated by current numerical code and are given in Table A.2. Comparisons presented in Table A.2 show and lend credibility to our numerical predictions for flow and temperature fields without considering radiative heat transfer.

Table A.2 Comparison of f Re and Nu for fully developed flow in a square channel

Parameters	Shah and London	Present numerical model	Percent difference
f Re	56.908	57.048	0.246
Nu	3.091	3.0945	0.129

The three-dimensional rectangular box like furnace ($2m \times 2m \times 4m$) of Chai et al. was chosen as the next benchmark problem to validate the radiative heat transfer part of the code because they applied a finite volume method to absorbing and emitting medium with heat source. They considered a medium with extinction coefficient of $\beta = 0.5m^{-1}$ and a heat generation of $q_g = 5kW/m^3$. The following boundary conditions are used in this calculation:

$$z = 0: \quad T_w = 1200K \quad \varepsilon = 0.85$$
$$z = 4m: \quad T_w = 400K \quad \varepsilon = 0.70$$
$$all\ other\ walls: \quad T_w = 900K \quad \varepsilon = 0.70$$

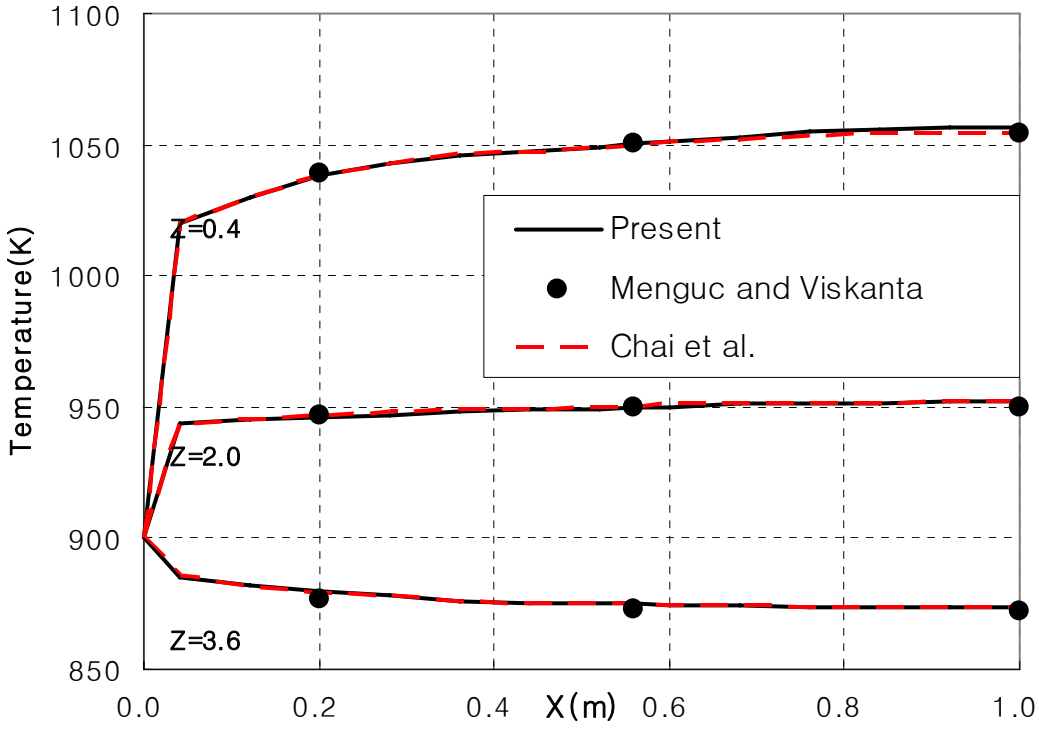

Figure A.3. Temperature distribution at y=1m

Once the blackbody intensity is calculated using Eq. (A.4), the medium temperature can be obtained using

$$E_b = \pi I_b = \sigma T_g^4 \tag{A.27}$$

The temperature distributions at $y = 1m$ and $x = 0.4, 2.0, and\ 3.6m$ of the furnace are compared with those predicted by Chai et al. and Menguc and Viskanta. Computations were performed on $25 \times 25 \times 25$ uniform control volumes and 8×24 control angles. Figure A.3 shows that the numerical results very closely agree with those using the finite volume method of Chai et al. and the P_3-approximation of Menguc and Viskanta. Thus validates our code.

For grid independence study a reference case of uniform grid with Re=400, Pr=0.7 was chosen. To consider various radiative effects we also chose absorbing, emitting, and anisotropic backward scattering medium. For phase function B Table A.1 was used. Also, the following quantities were used, : $\kappa = 0.5, \sigma = 0.5, T_w = 300K$, and $T_{in} = 1,000K$.

The average Nusselt number distribution was monitored with increase in grid size and results are presented in Table A.3. The relative percent difference in average Nusselt number for $60 \times 30 \times 30$ and $75 \times 38 \times 38$ is less than 0.02%. Accordingly, we chose $60 \times 30 \times 30$ uniformly spaced grid in this study.

Table A.3 Grid independence study for Re=400 and Pr=0.7

Grid size	Total number of cells	Percent difference in number of cells	Nu	Percent difference in Nu
30×15×15	6,750		4.4873	
40×20×20	16,000	137.037	4.4170	1.5666
50×25×25	31,250	95.313	4.3757	0.9350
60×30×30	54,000	72.800	4.3501	0.5850
75×38×38	108,300	100.556	4.3252	0.5724

A.7 Results and Discussion

A.7.1 Effect of Reynolds Number on Bulk Temperature and Nusselt Number

The effect of the Reynolds number (Re=200, 300, and 400) on the temperature distribution of the non-scattering medium with τ_{DH} =0.1, $T_w = 300K$, $T_{in} = 1,000K$ is shown in Figure A.4. For the case of Re=400 compared to Re=200, the bulk temperature and Nusselt number gradually decreased from inlet to outlet. It is evident that because of the inlet velocity augmentation for Re=400, the fluid flows faster and the radiation effect on temperature field diminishes. This result is clear when we change the energy equation, Eq. (A.3) into the dimensionless form, Eq. (A.28) as presented by Chai et al.

$$\frac{\vec{V}}{U_{in}} \cdot \left(\nabla \frac{T}{T_{in}} \right) = \frac{1}{\mathrm{Re}\,\mathrm{Pr}} \nabla^2 \left(\frac{T}{T_{in}} \right) - \frac{\kappa \beta D_h^2}{\mathrm{Re}\,\mathrm{Pr}\,N_{cr}} \left(\left(\frac{T}{T_{in}} \right)^4 - G \right) \qquad \text{(A.28)}$$

Note in radiative source term appeared on the second term of right-hand side and an increase in Reynolds number decreases the radiation effect.

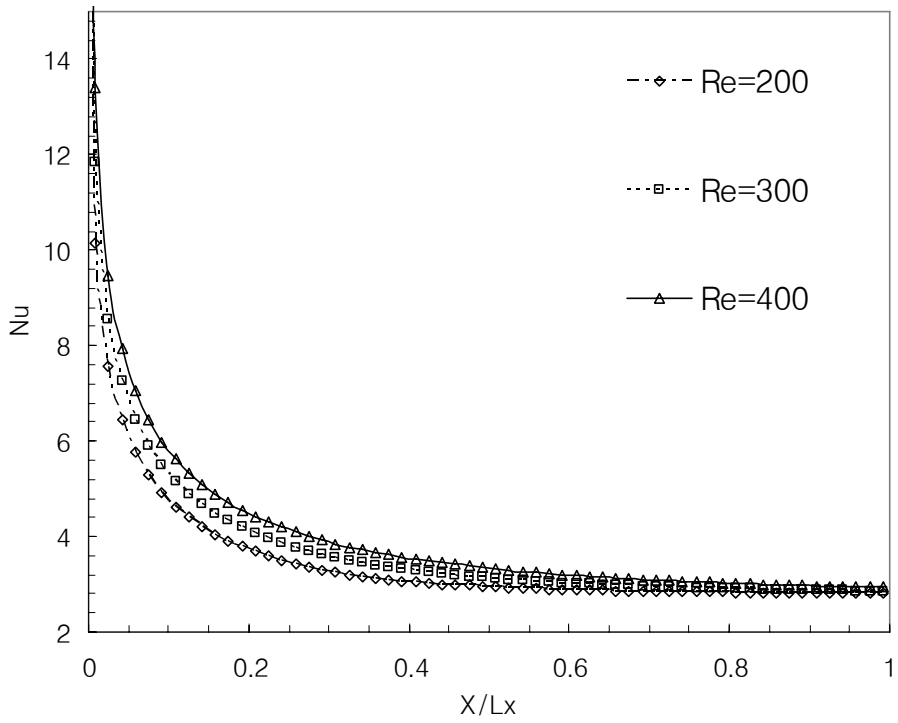

(a) Nu

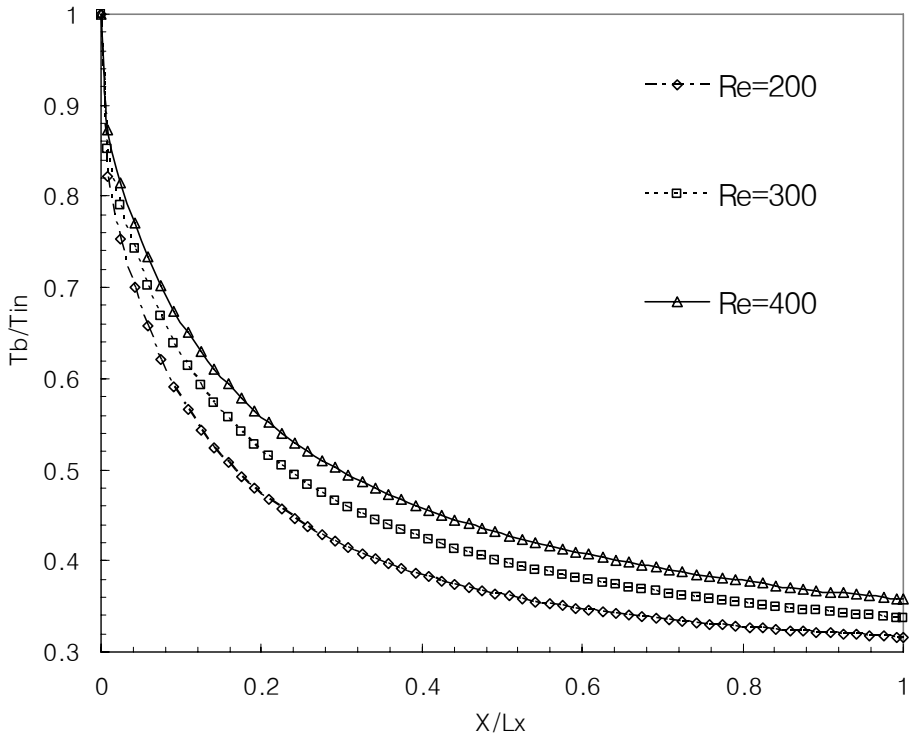

(b) Dimensionless bulk temperature

Figure A.4 Effect of Reynolds number (Re=200,300, and 400)

A.7.2 Effect of Conduction-Radiation Parameter on Bulk Temperature

The dimensionless bulk temperature distributions for combined mode heat transfer are calculated in the system with the assumption of a non-scattering medium, τ_{DH}=1 and Re=300. T_{in} depends on conduction-radiation parameter and $T_w = 0K$ is imposed at walls to simulate the large temperature variation between wall and inlet. This is shown in Figure A.5 for different values of conduction-radiation parameters (N_{cr}=0.001, 0.01, 0.1, and 1) and without radiation. The simulation for N_{cr}=1 is very similar to the simulation without radiation. With a decrease in conduction-radiation parameter, the extent of thermal penetration decreases. This is attributed to the fact that radiation enhances the heat transfer when there is a large variation in temperature between the inlet and the walls. Hence, the medium reaches the wall temperature rapidly with an increase in conduction-radiation parameter. Thus the conduction-radiation parameter has significant effect on temperature field.

A.7.3 Effect of Absorption Coefficient

Figure A.6 presents the temperature distribution for absorption coefficient (κ=1, 5, and 10) with N_{cr}=0.01, Re=300, and $T_w = 300K$. The effect of absorption coefficient on temperature profiles is shown to be of considerable significance. It reveals that with an increase in absorption coefficient, radiation is a dominant mode of heat transfer and the

bulk temperature and the penetration depth had steeper gradients. As expected, the fluid participates in the radiation transfer process by absorbing more energy radiated from the wall and emitting more energy to the medium at a higher absorption coefficient. Hence, the medium approaches the wall temperature at a much shorter distance from the entrance at higher absorption coefficient.

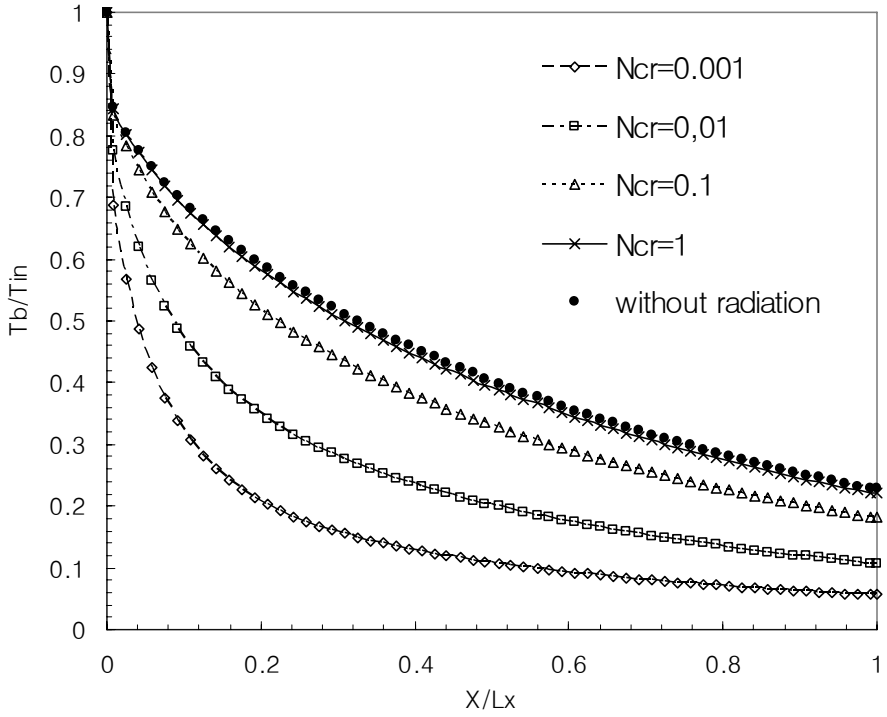

Figure A.5 Effect of conduction-radiation parameter (N_{cr} =0.001, 0.01, 0.1, 1, and no radiation)

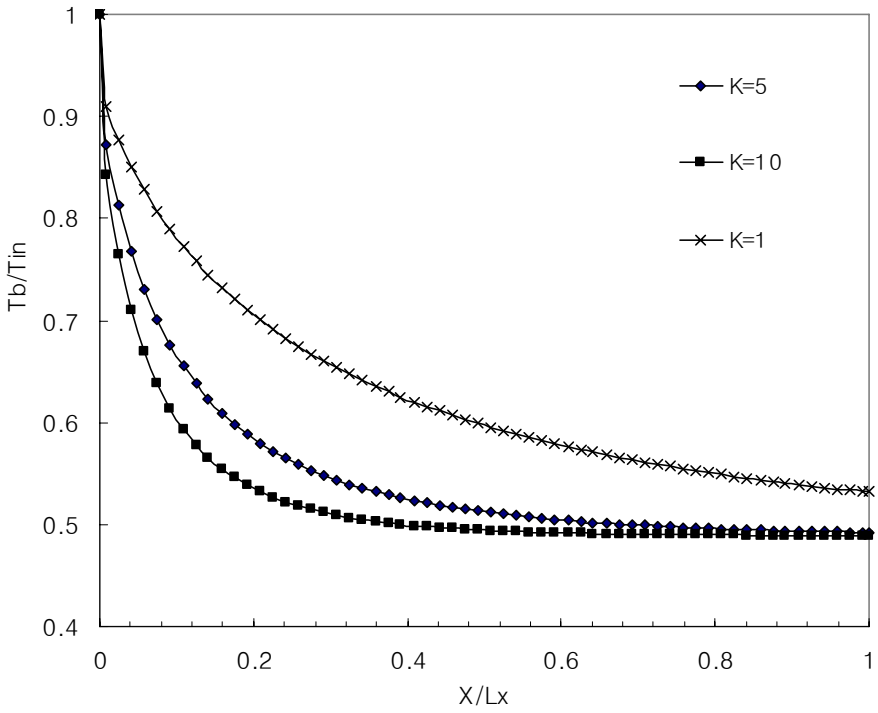

Figure A.6 Effect of absorption coefficient (κ=1, 5, and 10)

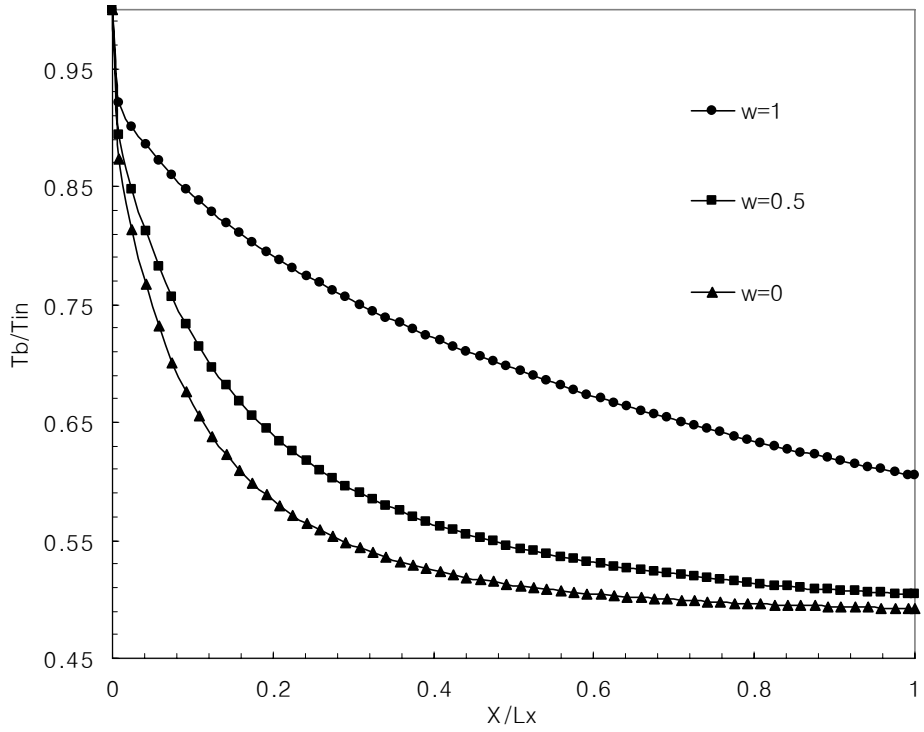

Figure A.7 Effect of scattering albedo (ω=0, 0.5, and 1)

A.7.4 Effect of Scattering Albedo

The effect of scattering albedo (ω=0, 0.5, and 1) on the temperature distribution for isotropic scattering phase function F in Table 1, τ_{DH}=0.5, N_{cr}=0.01, and Re=300 is shown in Figure A.7. As we can see the definition of scattering albedo ($\omega = \frac{\sigma}{\kappa + \sigma}$), ω=0 means pure absorption, and ω=1 represents pure scattering which means that the fluid does not absorb or emit radiative energy. From Figure A.7 increasing the scattering albedo increases the thermal penetration. This implies that increasing the scattering albedo enhances energy scattering by the medium. Hence, this results in increased thermal penetration. Bulk temperature increased with increase in scattering albedo.

A.8 Summary

A numerical simulation for combined heat transfer mode with participating medium was conducted using a finite volume technique to evaluate the temperature profile in a three-dimensional channel flow. Pressure and velocity fields were linked by the SIMPLE algorithm. The discretized equations were solved iteratively by the line-by-line method which is a combination of the Tri-Diagonal matrix algorithm and Gauss-Seidel scheme. The radiative heat transfer equation was also solved by a finite volume method. The energy equation with radiative source term was linearly discretized. The effects of Reynolds number, conduction-radiation parameters, optical thickness, and scattering albedo on average Nusselt number and the temperature distribution were presented.

Temperature distribution was influenced by radiation, depending on the absorption coefficient and the temperature difference between inlet and walls. The thermal penetration was influenced such that the fluid with a hot inlet compared to a cold wall was cooled in a relatively short distance from the channel inlet because of the radiation effect. With increasing Reynolds number, conduction-radiation parameter, scattering albedo, and decreasing optical thickness, the radiation effect is diminished, and thermal penetration is increased as a result.

A.9 References

1. J. C. Chai, H. S. Lee, and S. V. Patankar , Laminar Heat Transfer of a Radiating Fluid in a Backward Facing Step Flow, *Transport Phenomena in Thermal Engineering*, pp. 209-214, 1993.
2. J. C. Chai, H. S. Lee, and S. V. Patankar, Finite Volume Method for Radiation Heat Transfer, *J. Thermophys. Heat Transfer*, vol. 8, no. 3, pp. 419-425, 1994.
3. J. C. Chai, H. S. Lee, and S. V. Patankar, Improved Treatment of Scattering Using the Discrete Ordinates Method, *J. Heat Transfer*, vol. 116, pp. 260-263, 1994.
4. J. C. Chai, A Finite-Volume Methods for Radiation Heat Transfer, Ph.D. thesis, University of Minnesota, Minneapolis, 1994.
5. J. C. Chai and S. V. Patankar, Discrete-Ordinates and Finite-Volume Methods for Radiative Heat Transfer, *Handbook of Numerical Heat Transfer*, 2nd ed., ch. 9, pp. 298-309, 2006.

6. H. C. Chiu, J. H. Jang, and W. M. Yan, Mixed Convection Heat Transfer in Horizontal Rectangular Ducts with Radiation Effects, *Int. J. Heat Mass Transfer*, vol. 50, pp. 2874-2882, 2007.

7. E. H. Chui and G. D. Raithby, Computation of Radiant Heat Transfer on a Nonorthogonal Mesh Using the Finite Volume Method, *Numer. Heat Transfer*, vol. 23, pp. 269-288, 1993.

8. K. M. Im and R. K. Ahluwalia, Combined Convection and Radiation in Rectangular Ducts, *Int. J. Heat Mass Transfer*, vol. 27, pp. 221-231, 1984.

9. M. Kassemi and B. T. F. Chung, Conjugated Heat Transfer of a Radiatively Participating Gas in a Channel, *Proceedings of the Eighth International Heat Transfer Conference*, vol. 2, pp. 797-802, 1986.

10. T. K. Kim and H. S. Lee, Two-Dimensional Anisotropic Scattering Radiation in a Thermally Developing Poiseuille Flow, *J. Thermophys. Heat Transfer*, vol. 4, pp. 292-298, 1990.

11. N. Kim, N. K. Anand, and D. L. Rhode, A Study on Convergence Criteria for a SIMPLE-Based Finite Volume Algorithm, *Numer. Heat Transfer*, Part B, vol. 34, pp. 401-417, 1998.

12. T. K. Kim and H. S. Lee, Effect of Anisotropic Scattering on Radiative Heat Transfer in Two-Dimensional Rectangular Enclosures, *Int. J. Heat Transfer*, vol. 31, no. 8, pp. 1711-1721, 1988.

13. M. P. Menguc and R. Viskanta, Radiative Transfer in Three-Dimensional Rectangular Enclosures Containing Inhomogeneous, Anisotropically Scattering Media, *J. Quant. Spectrosc. Radiat. Transfer*, vol. 33, no. 6, pp. 533-549, 1985.

14. A. Mezrhab, H. Bouali, H. Amaoui and M. Bouzidi, Computation of Combined Natural-Convection and Radiation Heat Transfer in a Cavity having a Square Body at its Center, *Applied Energy*, vol. 83, pp. 1004-1023, 2006.

15. S. V. Patankar, *Numerical Heat Transfer and Fluid Flow*, Taylor and Francis, Philadelphia, 1981.

16. G. D. Raithby and E. H. Chui, A Finite Volume Method for Predicting Radiant Heat Transfer in Enclosures with Participating Media, *J. Heat Transfer*, vol. 112, pp. 415-423, 1990.

17. R. H. Shah and A. L. London, *Advances in Heat Transfer, Supplement 1: Laminar Flow Forced Convection in Ducts*, Academic Press, New York, 1978.

18. A. T. Wassel, Molecular Gas Radiation and Laminar or Turbulent Heat Diffusion in a Cylinder with Internal Heat Generation, *Int. J. Heat Transfer*, vol. 18, pp. 1267-1276, 1975.

VITA

Min Seok Ko was born in Incheon, South Korea in 1973. He received his B.S. in mechanical engineering from Inha University, South Korea in 2000. After graduation, he enrolled at Texas A&M University for his M.S. in Mechanical Engineering in the fall of 2000 and earnd his M.S. degree in 2004. His Master's coursework emphasis was on nonlinear elasticity and vibration. He completed this Ph.D. Program at Texas A&M University in the Department of Mechanical Engineering under the supervision of Dr. N. K. Anand in 2007. His research interests include numerical simulation of combined convective radiative flow and heat transfer.

Mr. Ko may be reached at 101-1903 Samsung APT, Sinsang-dong, Jung-gu, Incheon, South Korea. His email is mechmania@yahoo.com.